

Enhancing density functional theory using the variational quantum eigensolver

Evan Sheridan¹, Lana Mineh¹, Raul A. Santos¹, and Toby Cubitt¹

¹Phasecraft Ltd.

29th February 2024

Abstract

Quantum computers open up new avenues for modelling the physical properties of materials and molecules. Density Functional Theory (DFT) is the gold standard classical algorithm for predicting these properties, but relies on approximations of the unknown universal functional, limiting its general applicability for many fundamental and technologically relevant systems. In this work we develop a hybrid quantum/classical algorithm called *quantum enhanced DFT* (QEDFT) that systematically constructs quantum approximations of the universal functional using data obtained from a quantum computer.

We benchmark the QEDFT algorithm on the Fermi-Hubbard model, both numerically and on data from experiments on real quantum hardware. We find that QEDFT surpasses the quality of groundstate results obtained from Hartree-Fock DFT, as well as from direct application of conventional quantum algorithms such as VQE. Furthermore, we demonstrate that QEDFT works even when only noisy, low-depth quantum computation is available, by benchmarking the algorithm on data obtained from Google’s quantum computer.

We further show how QEDFT also captures quintessential properties of strongly correlated Mott physics for large Fermi-Hubbard systems using functionals generated on much smaller system sizes. Our results indicate that QEDFT can be applied to realistic materials and molecular systems, and has the potential to outperform the direct application of either DFT or VQE alone, without the requirement of large scale or fully fault-tolerant quantum computers.

Contents

1	Introduction	2
1.1	Density Functional Theory	3
1.2	Quantum computation	4

1.3	Quantum enhanced DFT	5
1.4	Previous work	7
1.5	Outline	8
2	Lattice DFT	8
3	The QEDFT algorithm	11
4	QEDFT examples	13
4.1	The Fermi-Hubbard dimer	13
4.2	More general Fermi-Hubbard models	17
5	Results	19
5.1	1D Fermi-Hubbard results	19
5.1.1	Numerical simulation results	20
5.1.2	Results from real quantum hardware data	22
5.2	2D Fermi-Hubbard results	22
5.3	Analysis of XC functionals and potentials	25
6	Conclusions	28
A	Computational methods	30
B	Error analysis of the XC functional	31
C	QEDFT in 1D	32
C.1	Emulation	32
C.1.1	Finite size scaling	36
C.2	Hardware	37
D	QEDFT in 2D	39
D.1	Emulation	39
D.1.1	Finite size scaling	41
D.2	Hardware	42

1 Introduction

Materials systems constitute large, interacting and inhomogeneous quantum many-body problems. As such, understanding and describing their properties is a notoriously difficult problem. Exact simulation of materials on classical computers is restricted to small system sizes. Quantum simulation on quantum computers promises precise computation of their dynamics, but remains out of reach of current hardware [1]. Instead, a number of well reasoned approximations across different time and length scales are used to make consistently reliable predictions.

1.1 Density Functional Theory

At the atomic scale, Density Functional Theory (DFT) [2, 3] is the predominant computational method used for computing groundstate electronic and structural properties for a broad range of atomic, molecular and materials systems. DFT computations have their basis in the Hohenberg-Kohn [2] and Kohn-Sham [3] theorems, which show that for any electronic structure Hamiltonian, there always exists a non-interacting Hamiltonian from which a groundstate density can be constructed that is identical to that of the full many-body system. Of course, the local – also known as Kohn-Sham (KS) – potential in this non-interacting Hamiltonian is itself determined by the many-body groundstate density. So finding the correct KS potential for a given system is at least as hard as the original many-body problem. In DFT, a way of getting around this is to approximate the energy, as a functional of the density. This energy functional $E[n]$, where n is the groundstate density, decomposes into four parts:

$$E[n] = T[n] + U_H[n] + E_{\text{ext}}[n] + E_{\text{xc}}[n]. \quad (1)$$

The kinetic energy term $T[n]$, the Coulomb (or “Hartree”) term $U_H[n]$, the external potential $E_{\text{ext}}[n]$, and the “exchange-correlation” (XC) term $E_{\text{xc}}[n]$. This latter term is essentially defined as everything not accounted for by the other terms:

$$E_{\text{xc}}[n] = E[n] - T[n] - U_H[n] - E_{\text{ext}}[n]. \quad (2)$$

The kinetic, Hartree, and external terms can be computed classically within KS DFT [3]. Meanwhile, $E_{\text{xc}}[n]$ only depends on the electron-electron interactions, so in principle is a universal functional that applies to every many-body electronic structure problem. However, since knowledge of this universal functional would allow all many-body problems to be solved, determining the exact form of this universal functional is believed to be intractable [4, 5].

Instead, in DFT, various heuristic approximations of the XC functional are used. Simple and compact approximations are often the most useful, interpretable and computationally efficient [6]. In its most common formulation, the algorithmic complexity of DFT scales as $\mathcal{O}(N^3)$, with N being the number of particles, whereas the full quantum many-body simulation scales exponentially in the particle number on classical computers.

However, the performance of DFT is intrinsically limited by the accuracy of the XC functional approximation. The most basic and best-known of these is the local density approximation (LDA), which is determined by exact computation of the homogeneous, non-interacting electron gas [7]. Other more sophisticated parameterisations exist and are used in modern DFT computations [6] with different levels of classical algorithmic complexity. Over more than 50 years, hundreds of approximate XC energy functionals

have been proposed [8], for both continuous basis sets as well as model Hamiltonians [9], and used in virtually every facet of atomistic materials modelling. This has resulted in the foundational papers of DFT becoming some of the most cited works in the scientific literature [10, 11] and the birth of the field of ab-initio materials design [12].

Despite these many successes, a number of challenges still remain: from choosing the most appropriate functional for each system, to the general failure of XC functionals when applied to strongly correlated systems. There are many functionals which have impressive records across broad material classes when predicting certain properties, while completely failing for others. For example, many functionals tend to struggle with describing bond disassociation: when electrons localise on ions as the inter-atomic distance is increased. And this is closely related to the misprediction of lattice constants in solids even when the electronic structure is qualitatively correct [13]. Moreover, for strongly correlated materials systems, the current generation of XC potentials often make qualitatively bad predictions for electronic and structural groundstate properties, let alone attaining quantitatively accurate results.

In recent years, quantum many body approaches such as the Dynamical Mean Field Theory (DMFT) [14] and quasiparticle self-consistent GW [15] approaches have alleviated these issues for some strongly correlated systems. In these approaches, the XC functional is not modified or updated; instead, exact quantum simulations for restricted regions of the Hilbert space are performed multiple times. However, this requires extensive classical computational power for each new material.

1.2 Quantum computation

Recently, quantum computing hardware has become sufficiently advanced to allow non-trivial demonstrations of quantum computation of groundstate properties. Many different quantum algorithms have been proposed for finding groundstates. However, the most widely studied on near-term quantum hardware is the variational quantum eigensolver (VQE) [16, 17]. At its heart, like many classical variational algorithms, VQE is based on the Rayleigh-Ritz variational characterisation of the eigenvalues of the Hamiltonian H :

$$\lambda_0(H) = \min_{|\psi\rangle} \langle \psi | H | \psi \rangle. \quad (3)$$

However, in contrast with classical variational algorithms, in VQE the state $|\psi\rangle$ is generated — and its energy $E(|\psi\rangle) = \langle \psi | H | \psi \rangle$ with respect to the Hamiltonian H measured — on a quantum computer. This requires that a suitable, efficiently preparable class of quantum states $|\psi(\vec{p})\rangle$ be chosen, with parameters \vec{p} over which to optimise. Because quantum computers are able to efficiently construct states that cannot be described or computed effi-

ciently on classical computers, VQE has the potential to outperform classical variational methods.

The accuracy of VQE results depends on whether this variational class contains a good approximation to the groundstate, and many different variational classes have been proposed and studied [18, 19]. The performance of VQE also depends on the success of the classical optimisation routine used to optimise the measured energy $E(|\psi(\vec{p})\rangle)$ over the parameters \vec{p} . Theoretically, good choices of the variational class and classical outer optimiser show promise in solving certain quantum many-body problems [20].

However, the current regime of noisy intermediate-scale quantum (NISQ) hardware is notoriously subject to significant rates of noise and error. The success or otherwise of VQE therefore also depends, crucially, on hardware noise. Although non-trivial VQE computations have now been demonstrated on real quantum devices [21], none have yet gone beyond system sizes that can be simulated on classical computers. Although the results reproduce the correct physical properties in these cases, the VQE *state* itself, as generated on the quantum computer, is not necessarily close to the true groundstate.

1.3 Quantum enhanced DFT

In this work, we introduce and benchmark a new hybrid quantum/classical approach to the many-body electronic structure problem: *quantum-enhanced DFT* (QEDFT), which combines the complementary strengths of DFT and quantum computation. Rather than using the quantum computer to find the groundstate itself, we instead use the quantum computer to approximate the XC functional, which is then fed into a classical DFT iteration. Thus the quantum computer is not tasked with finding the groundstate itself, but rather with steering the DFT iteration towards an accurate solution. In this work, we focus on using VQE for the quantum part of the QEDFT computation. But we note that our approach is general, and any other quantum groundstate approximation algorithm could be used in QEDFT.

We find that combining DFT and VQE in this way outperforms both Hartree-Fock DFT alone, and quantum VQE alone. Moreover, this remains the case even when the VQE computation itself is very noisy, and its output is far from the true XC functional. Despite the VQE output being quantitatively inaccurate, it captures key qualitative features of the exact XC functional that classical approximations struggle to reproduce. And this suffices to steer the DFT iteration to more accurate solutions than it would otherwise converge to.

To carry this out, the evaluation of the XC functional must be transformed into a groundstate computation suitable for VQE. At a high level, there are two possible approaches: we can compute the XC functional via VQE during the DFT loop, at the density in the current DFT iteration; we

call this the *online* approach. Or we can use VQE to approximate the entire universal XC functional in advance, and then use this VQE-computed XC functional in the DFT iteration; we call this the *offline* approach. There are pros and cons to each approach: the online approach only evaluates the XC functional at densities actually required during the DFT iteration; whereas the offline approach may compute it at many densities that are not actually needed. However, the online approach requires calling out to the quantum computer during the DFT computation, thereby limiting the speed of the DFT computation; whereas the offline approach decouples the quantum and classical computation. Moreover, since we are approximating the universal functional, in principle the VQE functional approximation only needs to be computed once, and thereafter the same functional can be used in multiple QEDFT computations.

For large systems, the XC functional is essentially a continuous object, whereas a quantum computer can only compute (or approximate) its value at a discrete set of points, with intermediate points approximated by interpolation. In principle, assuming the VQE algorithm were able to compute the exact value of the functional at any given point, the finer the discretisation the more accurate the functional approximation. However, the fact that a discretised functional is being computed has a significant benefit. The number of points in the discretisation corresponds directly to the size of the quantum system used in the quantum computation to compute the value of the functional. Therefore, even if the quantum hardware is too small to fit the full system being simulated, we can still use VQE to approximate the XC functional on the quantum computer at the finest discretisation that will fit on the device, and then use this in a DFT calculation of the groundstate density of the much larger system of interest.

Our empirical study shows that QEDFT has a number of advantages over both Hartree-Fock DFT alone, and VQE (or other purely-quantum) approaches alone:

1. QEDFT usually achieves better accuracy than either Hartree-Fock DFT alone, or quantum VQE alone.
2. QEDFT does not necessarily rely on quantitatively accurate quantum computations (eg high fidelity with the true groundstate), so it may provide a path to quantum advantage even when the quantum hardware is noisy.
3. QEDFT can be applied to large many-body systems on small quantum hardware, so it may still be able to provide a quantum advantage for real materials even while the available hardware is too small to fit a full quantum simulation of the material.

All of the numerics and hardware experiments across 1D and 2D Fermi-Hubbard systems serve to support these claims. We highlight a subset of

our results that illustrate the above claims. [Figure 2](#) shows that QEDFT achieves better accuracy than DFT Hartree Fock on the 1D Fermi-Hubbard chain. [Figure 4](#) support the claim that QEDFT succeeds even when the output of the quantum part of the computation is noisy and quantitatively inaccurate. [Figure 2](#) and [Figure 5](#) show results obtained for large 1D and 2D Fermi-Hubbard lattices using small quantum computations.

1.4 Previous work

The first studies of DFT and quantum computing analysed its computational complexity [4]. However, with the advent of readily available near-term devices, there have been a number of early studies of the development of hybrid quantum-DFT algorithms being applied to small molecules [22] and mid-gap defect states in solid state materials [23–25]. In these works, DFT is bootstrapped by VQE [16, 17] and quantum subspace expansions [26] by active space embedding methods, where the full KS space of electrons is partitioned into classical and quantum sections. There is also a formulation in the spirit of DFT in the Zumbach Maschke basis [27] that outlines a theoretical proposal to compute an approximation of the XC potential based on density matrix measurements that iteratively correct the single-particle density towards the true solution. For the fault tolerant framework, an approach has been proposed that could obtain accurate approximations to the XC functional that uses machine learning [28], but requires the use of quantum algorithms not suited for near-term devices.

Finally, two recent works [29, 30] apply the formalism of DFT to the 1D Hubbard model using quantum algorithms. In [29] the authors use VQE within the Levy-Lieb formalism of DFT to compute the groundstate properties of the Hubbard dimer, supplementing their technique with a quantum kernel that can learn the density functionals of observables. On the other hand, in [30], a mapping between the KS Hamiltonian and an auxiliary Hamiltonian is implemented on a quantum computer. The authors posit that solving the auxiliary system instead can result in computational speed up. This approach is then applied to 1D Hubbard chain of size $L = 8$ and a hydrogen molecular chain.

We also note that functional design for correlated lattice models has also been explored classically in the context of various lattice inhomogeneities. It was first used in semiconductor models [31], but it has since been more routinely applied to one dimensional Hubbard chains [9, 32–35], where exact parameterisations of the XC functional are available based on the Bethe Ansatz. In 2D, this approach has highlighted groundstate properties of large inhomogeneous sheets of graphene in a tight binding model with Hubbard type interactions, where the exact functional was parameterised using exact diagonalisation data [36]. Additionally, in recent years machine learning methods have been trained against exact results, showing utility for para-

meterising the XC functional for molecules [37–39] and also for the Hubbard model [40]. It is now clear that improving methods for XC functional design is a key factor in unlocking the full range of capabilities afforded by KS DFT.

1.5 Outline

In the rest of this paper, we describe the QEDFT algorithm in more technical detail, and apply it to a number of many-body lattice models. Lattice models are good systems to benchmark the approach on, as they allow direct comparison to other quantum algorithms which have largely been tested in the lattice setting. Furthermore, because quantum computers consist of qubits, fundamentally any quantum simulation must be reduced in some way to a discretised model. Thus a lattice formulation of QEDFT is required in any case, whether explicitly or implicitly.

In [Section 2](#), we review the formulation of DFT on lattices, which differs slightly from the more familiar continuum formulation of DFT. In [Section 3](#), we describe how the XC functional is transformed into a groundstate problem amenable to quantum computation. We also explain how a quantum treatment on small system sizes can be used to interpolate approximations of the XC functional, which can then be used in DFT for much larger system sizes. As a simple illustrative example, we first show in [Section 4](#) how our QEDFT approach looks for the Hubbard dimer and then extend this to more complex Fermi-Hubbard models. In [Section 5](#), we compare the performance of the QEDFT algorithm numerically with both (simulated) VQE, and with DFT under a number of choices of classical functional approximations. We also explore the qualitative features of the QEDFT functional and their contribution to the algorithm’s performance. In [Section 5.1.2](#), we run the QEDFT algorithm on the 1D Fermi-Hubbard model using VQE data obtained on Google’s quantum device.

2 Lattice DFT

We consider the general Hamiltonian for the following many-body fermionic system defined on a lattice \mathcal{L} ,

$$H = \hat{T} + \hat{H}_{\text{int}} + \hat{H}_{\text{ext}}, \quad (4)$$

where \hat{T} , \hat{H}_{int} and \hat{H}_{ext} are the non-interacting, interacting and external field contributions respectively. DFT enables the efficient solution of this problem [31], under the assumptions of non-interacting ν -representability of an auxiliary system to [Eq. \(4\)](#) and the linear coupling of \hat{H}_{ext} to the local density, using density functionals rather than wavefunctions. The validity of the DFT approach has applicability for any Hamiltonian which linearly

couples to an external field, which for example could be the electric field, but more generally takes the form

$$H_{\text{ext}} = \sum_{i \in \mathcal{L}} v_i^{\text{ext}} \hat{n}_i, \quad (5)$$

where v_i^{ext} is the external potential. The first Hohenberg-Kohn (HK) theorem establishes a one-to-one mapping [2] between the groundstate electron density, $n_i = \langle \psi_{GS} | \hat{n}_i | \psi_{GS} \rangle$, and the many body groundstate wavefunction, $|\psi_{GS}[n]\rangle$, which is a functional of the density. The second HK theorem states that the groundstate electron density minimises the energy functional [2]. It follows that the expectation value of any observable in the groundstate is uniquely defined as a functional of the groundstate density. For example, the groundstate energy functional is given by

$$E_{GS} = F[n] + \sum_{i \in \mathcal{L}} v_i^{\text{ext}} n_i, \quad (6)$$

where $F[n] = \langle \psi_{GS}[n] | \hat{T} + \hat{H}_{\text{int}} | \psi_{GS}[n] \rangle$ is known as the universal functional, as it doesn't depend explicitly on the external potential. The exact analytical form of this functional is not known for many fermionic systems of interest and requires the solution of many body problems that do not scale efficiently in the system size on classical computers. Routine approximations of $F[n]$ are made to allow for practical implementations of DFT. The error in the estimation of groundstate observables depends on the quality of those approximations.

A necessary reduction is then made from the original problem to an auxiliary non-interacting (KS) Hamiltonian [3] that is guaranteed to reproduce the groundstate properties of the original system only if the exact universal functional is used. This step is valid only if the original system is non-interacting ν -representable, i.e the groundstate density of the original interacting system can be obtained from a non-interacting one. Within this scheme, known as the KS approach, Eq. (6) is written as,

$$E_{GS}[n] = T_{NI}[n] + U_H[n] + E_{XC}[n] + \sum_{i \in \mathcal{L}} v_i^{\text{ext}} n_i, \quad (7)$$

where $T_{NI}[n]$ is the kinetic energy of the auxiliary non-interacting system, $U_H[n]$ is the Hartree energy, and $E_{XC}[n]$ is the exchange-correlation energy functional. By minimising Eq. (7), the Euler-Lagrange equations result in,

$$\frac{\partial E_{GS}}{\partial n_i} = \frac{\partial T_{NI}}{\partial n_i} + \frac{\partial U_H}{\partial n_i} + \frac{\partial E_{XC}}{\partial n_i} + v_i^{\text{ext}} = 0, \quad (8)$$

which has a solution that is the groundstate density. This equation is equi-

valent to a non-interacting system with an effective potential defined as,

$$\begin{aligned} V_i^{\text{KS}} &= v_i^{\text{ext}} + \frac{\partial U_H}{\partial n_i} + \frac{\partial E_{XC}}{\partial n_i} \\ &= v_i^{\text{ext}} + V_H[n_i] + V_{XC}[n_i], \end{aligned} \quad (9)$$

where $V_H[n_i]$ is the Hartree potential and $V_{XC}[n_i]$ is the exchange correlation potential, which is the object that is typically approximated. The effective non-interacting single-particle system is known as the KS Hamiltonian,

$$\hat{H}_{KS} = \hat{T} + \sum_{i \in \mathcal{L}} V_i^{\text{KS}} \hat{n}_i. \quad (10)$$

This system of equations is then solved self-consistently where at each iteration the groundstate density at site index i is constructed from the eigenvectors of the KS system, by summing over the occupied single particle states of the KS eigenvectors (accounting for spin),

$$n_{GS,i} = 2 \sum_j^{\text{occ}/2} |\phi_j(i)|^2, \quad (11)$$

where $\hat{H}_{KS}\phi_j = \epsilon_j\phi_j$ is the full eigensolution of the KS system. Here we treat the example spin unpolarised lattice DFT, but we note that spin polarised lattice DFT can be treated by separating the Kohn-Sham states into their up and down spin channels. The groundstate energy of the original many-body system in terms of the KS eigenvalues and density is given by,

$$E_{GS}[n_{GS}] = 2 \sum_{i \leq \text{occ}/2} \epsilon_i - \sum_{i \in \mathcal{L}} V_{XC}[n_{GS,i}] n_{GS,i} - E_H[n_{GS}] + E_{XC}[n_{GS}]. \quad (12)$$

The KS solution is converged self-consistently by iteratively updating the input density by computing Eq. (11) and mixing it with the previous density estimate,

$$n^{(j+1)} = \alpha n^{(j)} + (1 - \alpha) n^{(j+1)} \quad (13)$$

where j is the DFT iteration index and α is a linear mixing parameter that is used for numerical stability. When the groundstate observables no longer change up to a tolerance δ then the groundstate energy and density are equivalent to those of the interacting problem, if the true XC energy functional is used.

To summarise, the groundstate density minimises the total energy functional which enforces the functional derivative to be zero and results in a variational equation for auxiliary wavefunctions that can construct the groundstate density. This equation takes the form of a single-particle equation which can be treated as a standard eigenvalue problem. All of many-body physics manifests in the exchange correlation potential contribution

Algorithm 1: The lattice DFT algorithm

Choose the inhomogeneous representation (i.e the external potential) of the fermionic system to be used [Eq. \(4\)](#)

1. Choose initial density;
 2. Construct the KS potential [Eq. \(9\)](#) where V_{XC} is approximated;
 3. Solve for (ϕ_j, ϵ_j) in the KS system of equations $\hat{H}_{KS}\phi_j = \epsilon_j\phi_j$ with \hat{H}_{KS} [Eq. \(10\)](#);
 4. Construct density estimate from the KS eigenvectors [Eq. \(11\)](#);
 5. Compute energy of the system [Eq. \(12\)](#);
 6. Check for system convergence;
 7. If converged, exit loop and compute groundstate properties. If not, go back to step (1) and use new estimate of density as the input density [Eq. \(13\)](#);
-

Table 1: The algorithmic procedure for executing a DFT loop for practical applications.

of an otherwise fully determined effective single particle potential. These equations are solved self consistently, as the XC potential depends on the density, and the density depends on the unknown auxiliary wavefunctions. At self consistency, these wavefunctions no longer change and are used to construct groundstate observables, most notably the density and energy. The algorithmic procedure is presented in [Table 1](#).

3 The QEDFT algorithm

In this section we present the quantum-enhanced DFT algorithm for fermionic systems within the lattice DFT formalism presented in [Section 2](#). The main difference between lattice DFT and normal (ab initio) DFT is that the former is discrete, while the latter uses continuous basis sets. The algorithm consist of two parts (a) the computation of the XC potential and energy using a quantum machine and (b) application of the potential and energy within a DFT loop, which essentially follows the steps outlined in [Section 2](#). We discuss QEDFT in its offline mode, where the quantum computer is called during the first stage only and the second stage is a purely classical computation that queries that results from the first stage. Our approach is motivated by the deficiencies of classical DFT approximations to

systematically incorporate the effects of exchange and correlations. On the other hand, quantum computations natively include these effects, so building functionals out of their computations has the potential to improve upon classical approximations.

In [Table 2](#) we describe the algorithmic procedure for computation of the quantum-enhanced XC (QE-XC) potential and energy in this scheme. The initial step of the problem is to choose a homogeneous system of size L . The homogeneous Hamiltonian is related to the inhomogeneous Hamiltonian of [Eq. \(4\)](#) by setting $\hat{H}_{\text{ext}} = 0$. Its groundstate energy for density $n = \{n_1, \dots, n_L\}$ is given by the universal functional $F[n = \{n_1, \dots, n_L\}]$, where $\sum_i n_i = N_e$ corresponds to the total number of electrons in the system. The fermionic Hamiltonian of L sites is then encoded into a $M = \mathcal{O}(2L)$ qubits Hamiltonian via a fermion-to-qubit mapping,

$$H^{\text{fermions}} = \sum_k h_k \rightarrow H^{\text{qubits}} = \sum_\alpha \lambda_\alpha P_\alpha, \quad (14)$$

where $P_\alpha \in \{I, X, Y, Z\}^{\otimes M}$ are Pauli operators and λ_α are real coefficients. This mapping is necessary due to how operations are executed on the quantum device and its choice depends on the system under consideration.

A quantum circuit representation $|\Psi_{QC}[n]\rangle$ is then created that can be used by quantum algorithms to predict the groundstate energy of the system for a fixed number of fermions. The variational quantum eigensolver ([Section 1.2](#)) can be used for this step, where a quantum circuit is parameterised by real parameters that are variationally optimised for. At each allowed fermionic filling, the quantum algorithm is run to compute the groundstate energy,

$$E(n) = \langle \Psi_{QC}[n] | H^{\text{qubits}} | \Psi_{QC}[n] \rangle \quad \text{where} \quad \sum_i n_i = N_e, \quad \forall N_e \in \{0, \dots, 2L\}. \quad (15)$$

At this stage, there is still the combinatorially many possibilities for the densities at each site of the lattice \mathcal{L} as $n = \{n_1, \dots, n_L\}$. To further reduce the complexity we employ the local density approximation, where we just scan over states with total density N_e/L . This naturally fits in the state preparation of $|\Psi[n]\rangle$ as the total density is a conserved quantity, so the VQE minimization rearranges the local density profile while maintaining N_e .

From now on, within the offline QEDFT mode all computations are executed on a classical machine that post-processes the function $E(n)$ with a spacing $1/2L$. We introduce the quantum-enhanced local density approximation ϵ_{QELDA} for the energy [Eq. \(15\)](#),

$$\epsilon_{QELDA} \left(\frac{N_e}{L} \right) = \frac{E(n)}{L}, \quad \text{s.t.} \quad \sum_i n_i = N_e, \quad (16)$$

over the domain $\frac{N_e}{L} \in [0, 2]$. Therefore, as the system size is increased, the number of grid points that can be accessed by $\epsilon_{QELDA}(\frac{N_e}{L})$ increases and the resolution of the local energy increases. The local XC energy can also be obtained via,

$$\epsilon_{QELDA-XC}\left(\frac{N_e}{L}\right) = \epsilon_{QELDA}\left(\frac{N_e}{L}\right) - \epsilon_{HF}\left(\frac{N_e}{L}\right), \quad (17)$$

where $\epsilon_{HF}(\frac{N_e}{L})$ is the local Hartree Fock (HF) energy which can be obtained efficiently on a classical machine. In this representation, the total exchange correlation energy is approximated as a linear combination of the local energy generated by the local density at each site, i.e.

$$E_{QE-XC}(n) = \sum_{i \in \mathcal{L}} \epsilon_{QELDA-XC}(n_i). \quad (18)$$

The QE-XC potential is then obtained by taking the numerical derivative of Eq. (18),

$$V_{QE-XC}(n_i) = \left. \frac{\partial E_{QE-XC}(n)}{\partial n_i} \right|_{n=n_{GS}}. \quad (19)$$

As Eq. (19) and Eq. (17) are only known in the domain $[0, 2]$ with grid spacing $1/2L$ it is necessary to generate a continuous representation of it so that it can be queried in a DFT loop. This can be achieved by performing a spline interpolation for a fixed polynomial order. As a result of this interpolation, the functional can be used for target systems which are not the ones used to generate it. For example, a functional which is generated on a 2D system of size 3×3 can be used for a target system of size 30×30 . The DFT loop then proceeds as described in Section 2 for any Hamiltonian system given by Eq. (4), where the form of the XC potential and energy used in the DFT query is given by the continuous representations of Eq. (18) and Eq. (17).

4 QEDFT examples

In this section, we present some examples for how the QEDFT algorithm can be applied to the Fermi-Hubbard model.

4.1 The Fermi-Hubbard dimer

Here we will describe each of the necessary steps required for implementing the QEDFT algorithm for the prototypical 1×2 inhomogeneous Fermi-Hubbard model at half-filling. The model that QEDFT solves is:

$$\begin{aligned} H_{IH} = & -t(\hat{c}_{1\uparrow}^\dagger \hat{c}_{2\uparrow} + \hat{c}_{2\uparrow}^\dagger \hat{c}_{1\uparrow} + \hat{c}_{1\downarrow}^\dagger \hat{c}_{2\downarrow} + \hat{c}_{2\downarrow}^\dagger \hat{c}_{1\downarrow}) \\ & + U(\hat{n}_{1\uparrow} \hat{n}_{1\downarrow} + \hat{n}_{2\uparrow} \hat{n}_{2\downarrow}) \\ & + v_1(\hat{n}_{1\uparrow} + \hat{n}_{1\downarrow}) + v_2(\hat{n}_{2\uparrow} + \hat{n}_{2\downarrow}), \end{aligned} \quad (20)$$

Algorithm 2: Obtaining the quantum-enhanced XC potential and energy

Choose system of interest and construct its homogeneous fermionic Hamiltonian representation, i.e Eq. (4) where $\hat{H}_{\text{ext}} = 0$;

1. Encode the fermionic Hamiltonian into qubits via a fermion-to-qubit mapping Eq. (14);
 2. Create a quantum circuit representation for computation of groundstate energy;
 3. Use a quantum computer to compute the groundstate energy at each allowed fermionic filling (Eq. (15));
 4. Use a classical computer to obtain the exchange correlation energy Eq. (18);
 5. From the exchange correlation energy, compute the exchange correlation potential Eq. (19);
 6. Interpolate the exchange correlation potential and energy to obtain continuous representations and store on a classical computer.
 7. Use exchange correlation potential and energy in the DFT loop (Table 1) for any inhomogeneous fermionic Hamiltonian of the form Eq. (4).
-

Table 2: The algorithmic procedure to generate a classical representation of a quantum-enhanced XC potential and energy

where U is the interaction strength, t is the hopping amplitude, and $\{v_1, v_2\}$ are the chemical potentials for the different sites that constitute the external potential. This form of the inhomogeneous Hamiltonian corresponds to that of Eq. (4) for two sites. The homogeneous Hamiltonian that is required by the QEDFT algorithm (Table 2) is equivalent to Eq. (20) without the external potential, which is given by,

$$H_H = -t(\hat{c}_{1\uparrow}^\dagger \hat{c}_{2\uparrow} + \hat{c}_{2\uparrow}^\dagger \hat{c}_{1\uparrow} + \hat{c}_{1\downarrow}^\dagger \hat{c}_{2\downarrow} + \hat{c}_{2\downarrow}^\dagger \hat{c}_{1\downarrow}) + U(\hat{n}_{1\uparrow} \hat{n}_{1\downarrow} + \hat{n}_{2\uparrow} \hat{n}_{2\downarrow}). \quad (21)$$

Following the algorithmic protocol presented in Table 2, the Fermi-Hubbard dimer is first transformed from a complex fermionic representation to qubit representation via a fermionic encoding. Using the Jordan-Wigner encoding, the terms in the Hamiltonian are transformed as follows:

$$\hat{c}_i^\dagger \hat{c}_j + \hat{c}_j^\dagger \hat{c}_i \mapsto \frac{1}{2}(X_i X_j + Y_i Y_j) Z_{i+1} \cdots Z_{j-1}, \quad \hat{n}_i \hat{n}_j \mapsto \frac{1}{4}(I - Z_i)(I - Z_j), \quad (22)$$

assuming each spin-orbital has been assigned a unique index with a chosen Jordan-Wigner ordering (e.g. all up orbitals, followed by all down with the lattice sites in a snake ordering [41]). In the specific case of the half-filled dimer, it is possible to reduce the 4-qubit representation of the Fermi-Hubbard Hamiltonian into a 2-qubit one as only four amplitudes in the statevector are non-zero. The compressed representation is given by [42],

$$H_C = -t(X \otimes I + I \otimes X) + \frac{U}{2}(I + Z \otimes Z). \quad (23)$$

It has been shown in numerical simulations that one layer of the Hamiltonian variational ansatz [43] is required to find the groundstate of this model using VQE [41, 42]. Therefore, the state that we prepare using VQE is the following:

$$|\psi(\theta, \phi)\rangle = e^{i\theta(X \otimes I + I \otimes X)} e^{i\phi(I + Z \otimes Z)} |\psi_0\rangle, \quad (24)$$

where θ, ϕ are variational parameters, and $|\psi_0\rangle = |-\rangle \otimes |-\rangle$ is the groundstate of H_C with $U = 0$.

For each fermionic filling the groundstate energy at a fixed U/t needs to be computed, i.e $E(N_e, U/t) \forall N_e \in \{0, 1, 2, 3, 4\}$. For $N_e = 2$, VQE with the ansatz in Eq. (24) can be used. For $N_e = 0, 4$, the number sector is one dimensional and so a quantum computer does not need to be used. The energy for $N_e = 1$ can also be calculated classically using the observation that there are no interacting U terms which reduces the problem to one with hopping terms only. A similar argument can be used in the symmetric case of $N_e = 3$. The calculation of $E(N_e, U/t)$ allows then for the local XC energy to be calculated,

$$\epsilon_{QEDFT-XC} \left(\frac{N_e}{2}, U/t \right) = \epsilon_{QEDFT} \left(\frac{N_e}{2}, U/t \right) - \epsilon_{MF} \left(\frac{N_e}{2}, U/t \right) \quad (25)$$

where the QEDFT energy is found by obtaining the following energies on a quantum machine,

$$\epsilon_{QEDFT} \left(\frac{N_e}{2}, U/t \right) = \frac{E(N_e/2, U/t)}{4} \quad \forall N_e \in \{0, 1, 2, 3, 4\}. \quad (26)$$

The mean field energy can be computed classically by solving the non-interacting homogeneous Fermi-Hubbard model and computing:

$$\begin{aligned} \epsilon_{MF} \left(\frac{N_e}{2}, U/t \right) &= \frac{U}{2} (\langle \hat{n}_1 \rangle^2 + \langle \hat{n}_2 \rangle^2) \\ &\quad - t \langle (\hat{c}_{1\uparrow}^\dagger \hat{c}_{2\uparrow} + \hat{c}_{2\uparrow}^\dagger \hat{c}_{1\uparrow} + \hat{c}_{1\downarrow}^\dagger \hat{c}_{2\downarrow} + \hat{c}_{2\downarrow}^\dagger \hat{c}_{1\downarrow}) \rangle. \end{aligned} \quad (27)$$

Then, the QEDFT XC potential is found by taking the numerical derivative of Eq. (25) with respect to the density, as shown in Eq. (19).

Finally, the QEDFT XC potential is interpolated so that it can be queried at any density between 0 and 2. This concludes the first phase of applying QEDFT to the Fermi-Hubbard dimer which creates a classical queryable function that can be used in a DFT computation.

Now, having a continuous representation for the XC energy and potential we can return to solving Eq. (20) with lattice DFT according to the algorithm protocol of Table 1. Firstly, the density must be initialised and a common choice is to make it such that it is proportional to the external potential,

$$n_{\text{init}} \propto V_{\text{ext}} = (v_1, v_2). \quad (28)$$

The KS potential is then initialised for the two lattice sites,

$$\begin{aligned} V_1^{KS}(n_1) &= v_1 + \frac{U}{2}n_1 + V_{QEDFT-XC}(n_1) \\ V_2^{KS}(n_2) &= v_2 + \frac{U}{2}n_2 + V_{QEDFT-XC}(n_2), \end{aligned} \quad (29)$$

which allows for the full single particle KS Hamiltonian of the system to be expressed as,

$$\begin{aligned} H_{KS} &= -t(\hat{c}_{1\uparrow}^\dagger \hat{c}_{2\uparrow} + \hat{c}_{2\uparrow}^\dagger \hat{c}_{1\uparrow} + \hat{c}_{1\downarrow}^\dagger \hat{c}_{2\downarrow} + \hat{c}_{2\downarrow}^\dagger \hat{c}_{1\downarrow}) \\ &\quad + V_1^{KS}(n_{1\uparrow})\hat{n}_{1\uparrow} + V_1^{KS}(n_{1\downarrow})\hat{n}_{1\downarrow} \\ &\quad + V_2^{KS}(n_{2\uparrow})\hat{n}_{2\uparrow} + V_2^{KS}(n_{2\downarrow})\hat{n}_{2\downarrow}, \end{aligned} \quad (30)$$

where we have separated the spin channels, which we consider splitting into two independent problems as we deal with the spin unpolarised case by dealing with the total density at site i as $n_i = n_{i\uparrow} + n_{i\downarrow}$. The KS system of equations is then diagonalised, i.e $H_{KS}\phi_j = \epsilon_j\phi_j$, where ϵ_j are the KS eigenvalues and ϕ_j are the KS eigenvectors. Explicitly, for the Fermi-Hubbard dimer, the KS matrix for a given spin channel is, defined by,

$$H_{KS} = \begin{pmatrix} V_1^{KS}(n_1) & -t \\ -t & V_1^{KS}(n_2) \end{pmatrix}. \quad (31)$$

The spectrum of the KS problem consists of the eigenvalues $\{\epsilon_1, \epsilon_2\}$ and eigenvectors $\{\phi_1, \phi_2\}$, that are of dimension L . From the KS eigenvectors a new density is constructed, for the half-filled system this is:

$$\begin{aligned} n_1 &= 2|\phi_1(1)|^2, \\ n_2 &= 2|\phi_1(2)|^2, \end{aligned} \quad (32)$$

where $\phi_i(j)$ is the j^{th} element of the i^{th} KS eigenvector. This density is then used as the input to the next iteration of the DFT iterative algorithm, i.e.

Eq. (28) is replaced with these values. At each iteration the energy of the parent Hamiltonian, i.e. Eq. (20), is calculated using:

$$E_{GS}(\mathbf{n}^{GS}, U) = 2\epsilon_1 - V_{QEFT-XC}(n_1, U)n_1 - V_{QEFT-XC}(n_2, U)n_2 - \frac{1}{4}U(n_1^2 + n_2^2) + \epsilon_{QEFT-XC}(n_1, U) + \epsilon_{QEFT-XC}(n_2, U). \quad (33)$$

The algorithm concludes when the difference between the energy at two successive iterations is less than a chosen tolerance δ . At this point the results of the DFT algorithm for a chosen functional can be compared to the results produced via an exact method, which is possible as the Fermi-Hubbard dimer can be efficiently solved both analytically and numerically due to its small size.

4.2 More general Fermi-Hubbard models

We extend the dimer by adding more sites for a specified geometry to produce the generalised inhomogeneous Fermi-Hubbard model given by,

$$H = -t \sum_{\langle ij \rangle, \sigma} (\hat{c}_{i\sigma}^\dagger \hat{c}_{j\sigma} + \hat{c}_{j\sigma}^\dagger \hat{c}_{i\sigma}) + \sum_i^L U \hat{n}_{i\uparrow} \hat{n}_{i\downarrow} + \sum_i^L v_i^{ext} \hat{n}_i \quad (34)$$

where v_i^{ext} is the external lattice potential, U is the interaction strength, t is the hopping parameter and L is the system size. Here $\langle ij \rangle$ indicates a sum over nearest neighbours, and σ denotes the spin. KS theory then maps Eq. (34) into the effective KS system, where the many body interaction term is absorbed into a one-body potential V_i^{eff} ,

$$H_{KS, \sigma}(n_i) = -t \sum_{\langle ij \rangle} (\hat{c}_{i\sigma}^\dagger \hat{c}_{j\sigma} + \hat{c}_{j\sigma}^\dagger \hat{c}_{i\sigma}) + \sum_i^L V_i^{eff}(n_{i\sigma}) \hat{c}_{i\sigma}^\dagger \hat{c}_{i\sigma}, \quad (35)$$

for a given spin channel σ , which we now omit as we treat both spin channels equally going forward by setting the density variable as $n_i = n_{i\uparrow} + n_{i\downarrow}$. The effective KS potential for the generalised Fermi-Hubbard model is written as a combination of the external, Hartree, and XC potentials,

$$V_i^{eff}(n_i) = v_i^{ext} + \frac{U}{2}n_i + V_{QE-XC}(n_i). \quad (36)$$

$V_{QE-XC}(n_i)$ is the unknown XC potential, which is approximated according to the methods prescribed for Eq. (19) described in Table 2. Specifically, the XC energy for the Fermi-Hubbard model is,

$$E_{QE-XC}(n_i, U) = \frac{1}{L} E_{QE-hom}(n_i, U) - \frac{t}{L} \sum_{\langle ij \rangle \sigma} \langle \hat{c}_{i\sigma}^\dagger \hat{c}_{j\sigma} + \hat{c}_{j\sigma}^\dagger \hat{c}_{i\sigma} \rangle - \frac{1}{L} \sum_i^L \frac{U}{4} \langle n_i^2 \rangle \quad (37)$$

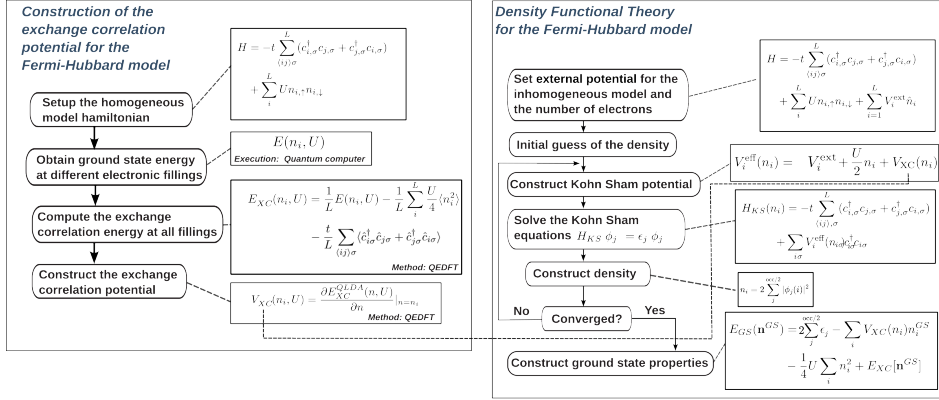


Figure 1: The general flow diagram of how the quantum and classical components interact in the QEDFT algorithm for the Fermi-Hubbard model. On the left hand side we illustrate how the exchange correlation potential is constructed within QEDFT. On the right hand side we show how the DFT loop is implemented within this hybrid scheme. We have highlighted by “Execution: Quantum Computer“ the computations which are run on the quantum computer, while the rest of the computations are all run on a classical computer.

where $E_{QE-hom}(n_i, U)$ is the energy of the homogeneous Fermi-Hubbard model, retrieved from Eq. (34) by setting $v_i^{ext} = 0$, and computed using VQE of a specified depth and occupation number. In the local density approximation the total homogeneous energy for the Fermi-Hubbard model is defined as the sum of the average energy in a homogeneous Fermi-Hubbard over the entire chain. Once Eq. (37) is computed and an ansatz for the initial density is made, the XC potential can be obtained by Eq. (19). This potential determines the KS system of equations to be solved. For example, for the 1D Hubbard chain with open boundary conditions, the KS matrix is

$$H_{KS} = \begin{pmatrix} V_1^{\text{eff}}(n_1) & -t & & & & & 0 \\ -t & V_2^{\text{eff}}(n_2) & -t & & & & \\ & -t & V_3^{\text{eff}}(n_3) & \ddots & & & \\ & & \ddots & \ddots & & & \\ & & & \ddots & \ddots & -t & \\ 0 & & & -t & V_{L-1}^{\text{eff}}(n_{L-1}) & -t & \\ & & & & -t & V_L^{\text{eff}}(n_L) & \end{pmatrix}, \quad (38)$$

The result of this diagonalisation are the KS eigenvalues, $\{\epsilon_1, \dots, \epsilon_L\}$, and the KS eigenvectors, $\{\phi_1, \dots, \phi_L\}$. The KS eigenvectors are used to construct a new approximation to the density via Eq. (11), which is then mixed with the previous density Eq. (13) for numerical stability, which can

be then used to construct a new KS matrix [Eq. \(38\)](#). At convergence the DFT approximation to the groundstate energy is,

$$\begin{aligned}
E_{GS}(\mathbf{n}^{GS}) = & 2 \sum_{i \leq \text{occ}/2} \epsilon_i^{KS} - \sum_{i \in \mathcal{L}} V^{XC}(n_i) n_i^{GS} \\
& - \frac{1}{4} U \sum_{i \in \mathcal{L}} n_i^2 + \sum_{i \in \mathcal{L}} E_{QE-XC}(n_i, U), \tag{39}
\end{aligned}$$

where only the first N_e KS eigenvalues are included in the summation, with N_e corresponding to the fermion filling of the inhomogeneous model [Eq. \(34\)](#). The entire protocol for the generalised Fermi-Hubbard system is illustrated in [Fig. 1](#).

5 Results

To test and validate the QEDFT algorithm described in [Section 3](#), we performed numerical simulations on classical hardware for 1D and 2D Fermi-Hubbard systems, and computations for 1D Fermi-Hubbard systems using data from Google’s Rainbow quantum hardware [\[21\]](#). We present these results in the following sections, followed by numerical results and analysis of the XC potentials produced by QEDFT and conventional DFT methods that gives insight into the performance of the QEDFT algorithm. The computational details used to generate these results are discussed in detail in [Appendix A](#).

5.1 1D Fermi-Hubbard results

In this section, we present results of the QEDFT algorithm for 1D Fermi-Hubbard systems, both in simulations and in computations using data from real quantum hardware, and comparing these to conventional DFT methods. 1D Fermi-Hubbard systems are readily solvable classically, both by analytic and numerical methods. The purpose of testing the algorithm on these systems is not, therefore, to compare the QEDFT performance to the best known classical methods, but rather to test the algorithm on well-characterised systems and assess (1) how close it gets to the correct solution, and (2) to compare its performance with classical DFT methods that scale to 2D and other systems (but which are not the optimal methods for 1D systems).

To obtain (good approximations) to the exact 1D solutions against which to benchmark, we use exact diagonalisation (ED) for system sizes small enough for this to be possible, and classical DFT with the BALDA functional [\[32\]](#) for system sizes beyond ED. The BALDA functional is based on exact solvability of the 1D Fermi Hubbard model in the thermodynamic limit. So although BALDA DFT is a classical DFT method, for finite 1D

Fermi Hubbard systems it is known to give results that are close to the exact solution.

For the 1D simulations, we take Hartree-Fock as a representative classical DFT method to compare and contrast QEDFT to. This is of course an artificial comparison, as 1D systems can be solved very effectively classically by other DFT methods such as BALDA DFT. But as QEDFT is a general method that is not tailored to 1D systems, it is useful to compare also to conventional DFT methods that are similarly generally applicable. Thus the comparison to Hartree-Fock DFT (HF) on 1D Fermi Hubbard systems allows us to gain insight into how QEDFT compares to conventional DFT methods that are applicable to general systems, but on a simple, well-characterised solvable model where we can also compare both to exact solutions.

Because the results in this section are obtained by simulating QEDFT (or more precisely, the VQE subroutine) on a classical computer, we can only compute the VQE functionals used in QEDFT on small lattice sizes. For such small lattices, simulated VQE with perfect quantum gates can readily find the exact ground state, so that QEDFT reduces to DFT with ED functionals. Therefore, in order to gain insight into how QEDFT performs when the VQE functionals are *not* perfect, which will always be the case when one runs VQE on real quantum hardware with lattice sizes that are beyond the reach of classical simulation, we deliberately hobble the VQE by restricting the VQE circuit depth such that it is not able to obtain the exact ground state.

5.1.1 Numerical simulation results

In Fig. 2 we show the results of applying QEDFT for a 1×200 instance of the Fermi Hubbard model using a functional generated by the emulation of VQE applied to a 1×12 Hubbard chain. In these simulations we use the BALDA functional as the exact benchmark, as performing ED simulations for these system sizes is not possible. The system parameters are $U/t = 10$ at quarter-filling ($N_e = 100$) within a confining quadratic potential $v_i^{\text{ext}} = (i - L/2)^2/L$, with $L = 200$. This model is known to exhibit regions of coexisting phases between metallic (compressible) and Mott insulating (incompressible) characteristics [32]. Such a scenario is illustrated in Fig. 2 in the BALDA density profile at the centre of the trap, where a plateau emerges and the density is constrained to $n_i = 1$. This plateau is determined by the competition between $v_i^{\text{ext}} + Un_i/2$ and V_{XC} in the KS potential, which are separated by the XC potential discontinuity at $n_i = 1$.

Importantly, the QEDFT methods capture the coexistence of the localised incompressible region with that of the metallic compressible phase, a key feature of the correlated regime. The correlated driven plateaus are entirely absent from the HF result and hence serve as a demonstration that low depth and low quality QEDFT functionals can be qualitatively superior

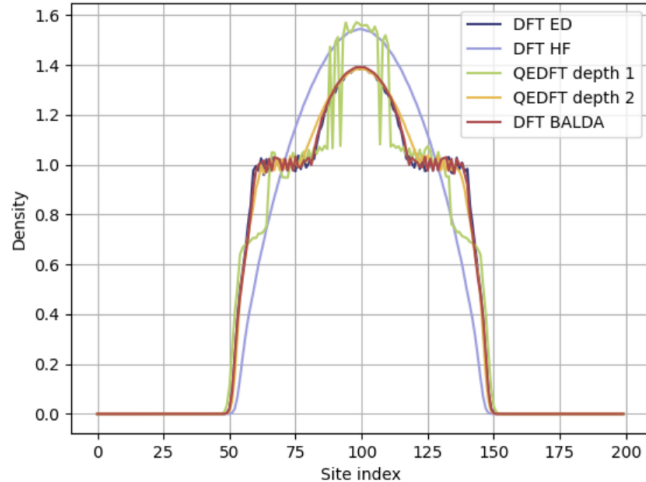


Figure 2: The ground state density of the 1×200 Fermi Hubbard model for $U/t = 10$ and at quarter filling within a confining quadratic potential using a QEDFT functional generated on a 1×12 homogeneous Fermi-Hubbard system. The presence of Mott plateaus, characteristic of correlations in the system, are captured by the shallow depth VQE functionals, albeit less so at depth 1. These features are absent in the Hartree Fock approach.

in their descriptive capabilities in the strongly interacting regime. Additional analysis of the energy convergence as function of the DFT iterations is presented in [Appendix C](#). These results give evidence that QEDFT usually achieves better accuracy than Hartree-Fock DFT its own, without requiring extremely accurate quantum computations.

To demonstrate that our emulated results are not valid only for a single U/t value, we present the effect of varying the interaction strength on the 1×200 system, shown in [Fig. 3](#). The errors are measured relative to the BALDA DFT method. Here we find that for all values of U/t examined the QEDFT densities are more accurate than the HF densities, and similarly for the ground state energy. This shows that for large 1D systems QEDFT based on restrictive quantum emulations achieves better results than HF DFT alone, for a system size currently well beyond the reach of standard quantum VQE. However, the accuracy deteriorates at larger interaction strengths, in particular for HF and QEDFT depth 1. This is related to the known issue of sampling near unity in the compressible phase with DFT methods that use functionals with XC discontinuities [32]. At $U/t = 10$ we see for QEDFT depth 1 that there is a jump in the density error, which we associate with the emergence of the Mott plateaus near the centre of the trap. For lower values

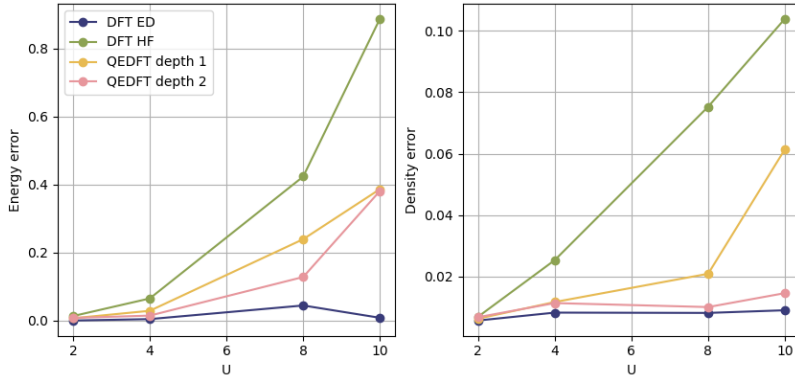


Figure 3: The 1×200 Fermi Hubbard model at quarter-filling with a quadratic external potential and its respective errors in energy (left panel) and density (right panel) for different interaction strengths. All simulations use DFT and the BALDA DFT functional is used as the exact benchmark.

of U/t , the QEDFT functionals are comparable and competitive with the essentially exact BALDA solution. Further supporting results are described in [Appendix C](#), in particular relating to smaller 1D systems and the effect of finite size scaling on the functional.

5.1.2 Results from real quantum hardware data

We also apply the 1×8 QEDFT functional derived from data taken on real quantum hardware, to the much larger 1×200 inhomogeneous Fermi-Hubbard model in the presence of an external quadratic potential at $U/t = 4$. Our parameter selection here was constrained by the parameter selections used for the hardware study [21]. We see in [Fig. 4](#) that the QEDFT hardware also captures the presence of Mott plateaus near $n = 1$, albeit less pronounced than our emulated results as in this case $U/t = 4$ instead of $U/t = 10$. Note that this feature is completely absent in the HF solution. These results give evidence that QEDFT is still able to give good solutions even in the presence of noise and errors that are inherent to running on real, pre-fault-tolerant quantum hardware.

5.2 2D Fermi-Hubbard results

Applying the functional generated in a small scale instance to an inhomogeneous larger system serves as a first step to make quantum-generated data on small devices useful for relevant applications. In order to test the validity of our results, we treat more challenging systems, where access to an exact functional is not possible. In this section, we present results of ap-

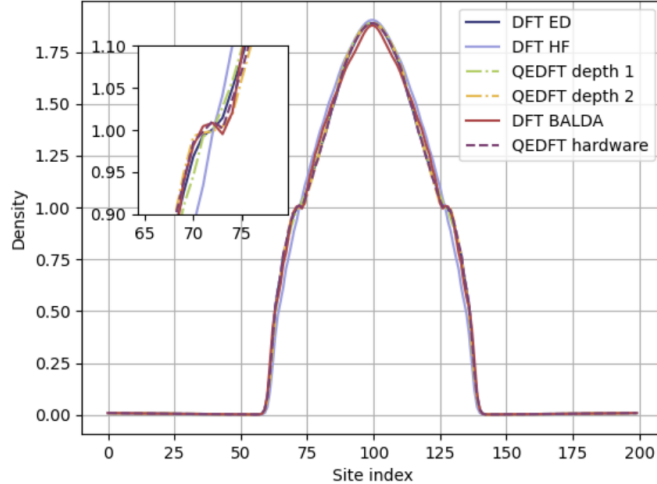


Figure 4: The ground state density of 1×200 Fermi Hubbard model for $U = 4$ at quarter filling within a confining quadratic potential using a QEDFT functional generated on a 1×8 homogeneous Fermi-Hubbard system from quantum hardware, as well as emulation. The inset highlights the region where the Mott plateaus emerge, which is the signature of correlations that are not captured with the HF approach.

plying QEDFT to 2D Fermi Hubbard systems, using classical simulations and computations using real hardware data, as well as computations using classical DFT methods.

We do this by extending our analysis to a 20×20 inhomogeneous Fermi-Hubbard system for $U/t = 4$ at quarter-filling. The inhomogeneities are generated by a cluster of impurities at the centre of the lattice in the presence of a weak background disordered potential. Exact solutions for this system would require diagonalising a matrix of dimensions $4^{20 \times 20} \times 4^{20 \times 20}$, which is not possible with classical computers. DFT, on the other hand, only requires the diagonalisation of a matrix with dimensions $(20 \times 20) \times (20 \times 20)$ which can be easily achieved. Fig. 5 shows the DFT densities for the 20×20 system using the 3×3 QEDFT XC functional (see Appendix D). It is clear that all of the DFT methods are able to distinguish where the impurities are located. The absence of an exact method for large 2D systems (unlike 1D systems where the BALDA functional exists, as well as other accurate 1D methods such as DMRG) means there is no exact ground truth comparison, and we choose to compare against the DFT ED method.

We see that the QEDFT functional of depth 2 is more in likeness to the DFT ED result, both in contrast to the classical HF functional and QEDFT

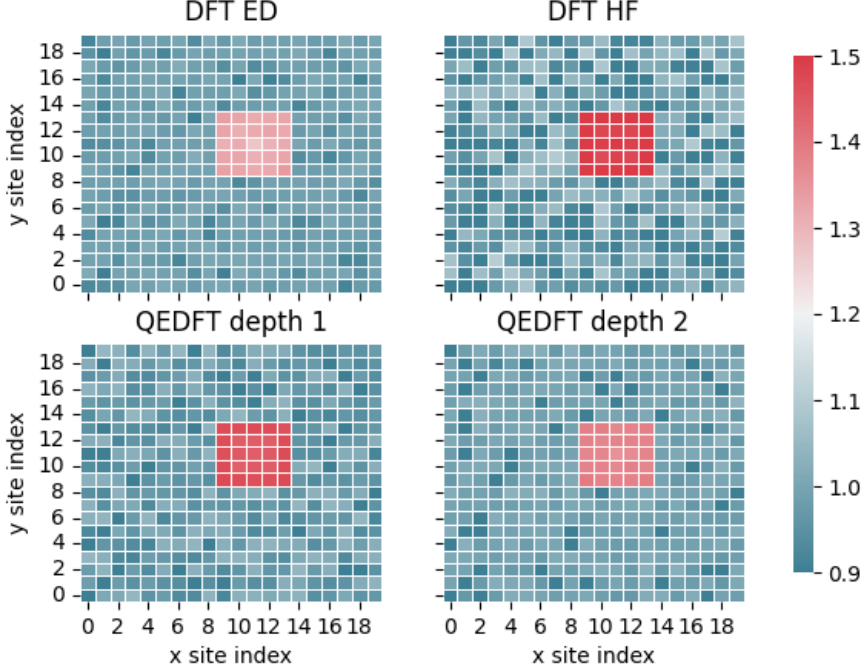


Figure 5: The density per site of the 20×20 Fermi Hubbard model at half-filling at $U/t = 4$ based on DFT calculations using functionals generated on a 3×3 lattice. The external potential is an impurity potential that concentrates fermions to a square at the centre of the lattice. As this model cannot be solved exactly, the DFT ED solution acts as an approximation to the ground state.

depth 1. Indeed, these results are comparable to the results we obtained for the densities of the 1×200 Fermi-Hubbard system, where QEDFT of depth 1 approximates the HF solution better than the exact solution. Thus, despite the lack of an exact solution for the ground state density, it is at least suggestive that QEDFT at depth 2 is incorporating effects that are not present in the HF solution. These results thus lend further support to the evidence that QEDFT, in this case applied to 2D Fermi-Hubbard systems, gives useful results even when only small quantum devices are available and where hardware noise and errors prevent good solutions being obtained by VQE. Further analysis and results, in particular computations using real hardware data, are given in [Appendix D](#), on smaller 2D systems as well as their finite size scaling.

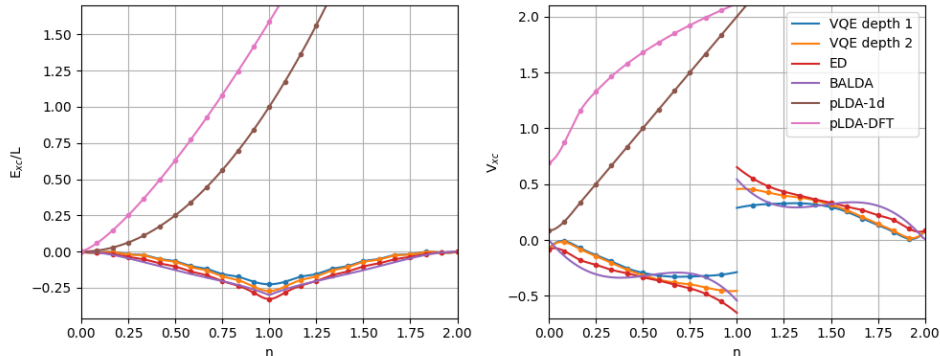


Figure 6: The XC energy (left) and potential (right) for the 1×12 Fermi-Hubbard model at $U/t = 4$ using different methods. The solid lines are produced using a cubic spline. The VQE results are obtained using a classical emulator. Note that the continuous LDA approximations perform badly in this system.

5.3 Analysis of XC functionals and potentials

Using the algorithm presented in Table 2, we generate the exchange correlation energies, from which we differentiate and apply a cubic polynomial spline to obtain the XC potential, as illustrated in Fig. 6. The purpose of generating these correlation functionals is to query them inside the DFT algorithm, hence the necessity for obtaining a continuous representation as a function of the number of electrons. To gain insight into how QEDFT and other DFT methods perform, it is therefore valuable to investigate and analyse the functionals that are generated by these different methods.

In order to do so, we must first discuss the general properties of the XC functionals for Fermi-Hubbard systems. The continuous lines in Fig. 6 represent cubic spline fits for each functional, where the XC potential is defined piecewise V_{XC}^{left} for $n \leq 1$ and V_{XC}^{right} for $n > 1$. We note that by replacing the discrete points with a continuous spline we introduce another source of approximate error, in addition and of different nature than the error introduced by approximating the XC functional. On the other hand, if the continuous representation is constructed on a dense enough mesh, and if the VQE depth is sufficient to within a desired error tolerance of the ED functional, then finite size physical errors, as well as those related to the interpolation scheme, can be reduced.

The XC potential has a discontinuity at $n = 1$ due to the cusp in the exchange correlation energy, commonly known as the derivative discontinuity (DD). The DD is a known property of the exact XC potential which a number of classical approximations fail to reproduce [44] and has consequences for the description of properties relating to the fundamental gap

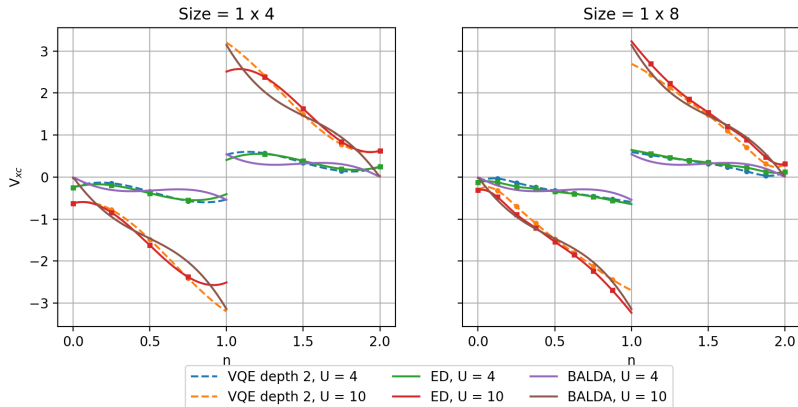


Figure 7: The effect of U/t and system size on the XC potential for 1D Fermi Hubbard models. Note that as U/t increases so to does the derivative discontinuity at $n = 1$ and by increasing the system size the mesh upon which the functional is splined becomes denser, reducing finite size errors.

of the system. All functionals presented in Fig. 6 exhibit this discontinuity, with the exception of the “pseudo“ functionals, and the depth 2 VQE functionals approximate this discontinuity with higher accuracy in regions both near and away from where the discontinuity occurs compared to depth 1. The “pseudo-DFT” functional, $E_{xc}(n) = 2^{-4/3}Un^{4/3}$ is based on the local density approximation applied in ab-initio methods, specifically for the homogeneous electron gas, and evidently is not a good approximation for the Fermi-Hubbard system. Similarly, the “pseudo-1D” functional, $E_{xc} = 0.25Un^2$, originates from the 1D equivalent. Not only do these functionals omit the DD but they also qualitatively arrive at values which are not comparable for either the XC energy or the XC potential. As these pseudo functionals are so erroneous - which we find is also the case in 2D - we chose not to analyse or implement them as part of the DFT study. We emphasise that the BALDA functional is valid in the limit of an infinite chain, but indeed the results for the 1×12 chain approximate this behaviour.

Having established that it is possible to generate the XC potential using VQE, in Fig. 7 we analyse the effect that different parameters, *i.e* correlation strength and system size, have on the resulting functionals. We observe that VQE functionals qualitatively agree with the ED and BALDA results, *e.g* capturing the DD and its general shape, but deteriorate quantitatively as the interaction strength increases. However, as the initial VQE state preparation corresponds to the $U = 0$ configuration, there are expected inaccuracies of the VQE circuits used for larger interaction strengths. Further detailed analysis that supports these observations is also presented in Appendix B. We see that the continuous representation is constructed on a denser mesh

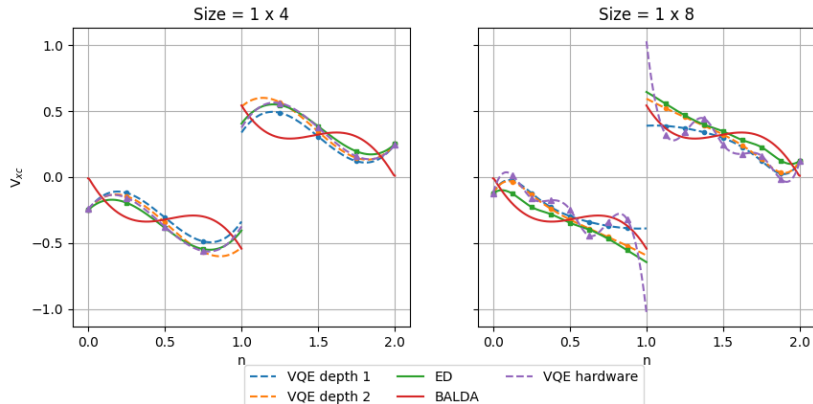


Figure 8: The effect of system size on the XC potential for 1D and 2D Fermi Hubbard models at $U/t = 4$ run on quantum hardware and classical simulations. Note that for the 1×4 system the quantum hardware functional is competitive with classical ED, while the presence of noise becomes apparent in the larger 1×8 hardware results.

for larger systems, as illustrated via the comparison of the 1×8 and 1×12 functionals. Thus if the VQE functional is generated on finer meshes for sufficient depth, then finite size physical errors, as well as those related to the interpolation scheme, can be reduced.

In Fig. 8 we show the VQE functional properties at fixed $U/t = 4$ across different system sizes for real quantum hardware data, details of which are specified in Appendix A. The 1×4 system shows the most accurate results, where the hardware results consistently fall between the simulated VQE depth 2 and DFT ED XC potentials. However, as the system size is doubled to 1×8 there is the manifestation of noise in the hardware functional, which has effects on both the raw data as well as creating oscillations in the subsequent interpolation, in particular in the density region near 1, so much so that it artificially enhances the DD by a factor of 2. Therefore, while we have shown that it is possible to generate competitive XC functionals using real hardware, the quality of the functionals worsens as the system size increases, due to noise in the measurements.

We furthermore extend the analysis of the effect of system size and interaction strength to VQE functionals generated on 2D lattices, shown in Fig. 9. As the Bethe ansatz applies only in 1D, we do not compare to the BALDA functional in 2D. We highlight that the curvature and DD of the functional in 2D attains a different quality and is visibly different in character for the configurations studied, e.g the 3×3 functional exhibits steps near $n = 1.5$ and $n = 2$, while 2×6 is mostly monotonic. There is a degradation of the functional near half-filling at $U/t = 10$ which is present

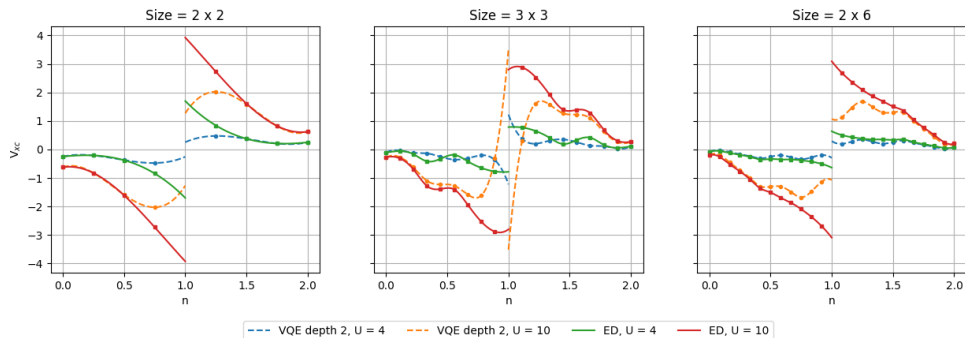


Figure 9: The effect of U and system size on the XC potential for 2D Fermi Hubbard models. The accuracy of the 2D VQE XC potentials at depth 2 is worse when compared to their 1D counterparts. In particular, for low interaction strengths their accuracy is competitive with classical ED, but there are larger errors for stronger interactions.

in each 2D emulated functional that impacts the continuous representation, particularly noticeable for the 3×3 system. However, there is considerably better agreement at $U/t = 4$, indicating that low-depth functionals can approximate the ED functionals for lower values of the interaction strength in 2D, with additional evidence explored in [Appendix B](#).

6 Conclusions

Density Functional Theory is the de facto standard for simulating molecular and materials groundstate properties on traditional computers. Its overwhelming popularity and success relies on choosing appropriate classical approximations to the unknown exchange correlation energy functional on a system-by-system basis. For many cases, especially those with strongly correlated electrons, the classical approximations are inadequate, and sophisticated approaches beyond DFT are needed that are not efficiently scalable on traditional computers. Simulating materials is regarded as a promising application for quantum computers [1] and has so far largely been viewed through the lens of hybrid quantum/classical algorithms to make the most of near-term noisy quantum resources. In this work we have introduced a new hybrid quantum/classical approach called *quantum-enhanced DFT* (QEDFT) that combines DFT with quantum computation. We have presented this formalism in generality within the specific framework of lattice DFT and applied it to various instances of the 1D and 2D Fermi-Hubbard models. Low depth VQE simulations and hardware experiments are used to construct approximations to the XC energy functional, which are then available to be used as part of the DFT algorithm.

In the majority of cases considered, QEDFT outperforms pure quantum

VQE alone, with respect to the accuracy of the groundstate energy and density of both the 1D and 2D inhomogeneous Fermi-Hubbard model. It also provides ground state properties which are more accurate than classical Hartree Fock theory. QEDFT captures exact properties of the XC potential functional, such as the derivative discontinuity at half-filling, which are not present in many well-known classical approximations. The derivative discontinuity and groundstate properties from QEDFT show impressive robustness to hardware noise and shallow variational layers. A hallmark of the QEDFT method is that it does not rely on highly accurate quantum computations to produce groundstate properties of either inhomogeneous or homogeneous lattice systems. Another quintessential feature is that QEDFT can be applied to large many-body condensed matter systems using only small quantum hardware. We achieve this by generating continuous representations of the QEDFT XC potential using classical interpolation schemes. In particular, we have shown this by solving 1×200 and 20×20 Fermi-Hubbard models using QEDFT, demonstrating that shallow VQE functionals of at most two variational layers can unambiguously capture Mott plateaus in the groundstate densities of large inhomogeneous models. We have also shown that our results improve by increasing the system size that the XC potential is generated from, highlighting that our approach can benefit from running quantum simulations on larger devices.

Extending the application of QEDFT beyond Fermi-Hubbard models to realistic atomic systems requires broadening the scope of the inhomogeneous Hamiltonians under consideration. In particular, the inclusion of additional effects is imperative to enhance the descriptive capabilities of QEDFT functionals to capture a rich variety of important physical processes such as multiorbital couplings, beyond nearest-neighbour interactions, lattice connectivity, and electron-phonon interactions, to name only a few important effects. Another important consideration for realistic systems is the effect of the underlying basis set used to represent continuous inhomogeneous models. This choice is well known to have significant technical consequences for how to setup the DFT problem and has recently also been explored in the context of quantum simulation [1, 45]. The basis set will also be an important consideration when building the QEDFT XC functionals that are used for real atomic systems, as the optimal representation of the homogeneous problem is needed to construct it. Additionally, including non-local effects from the density into the QEDFT functional, in the spirit of the classical GGA [46] approximation, presents complementary ways in which the QEDFT method can be improved upon when applied more generally.

In conclusion, QEDFT presents a new way in which to bring together DFT with quantum simulation, that is applicable across a broad range of physical fermionic Hamiltonians describing real atomic, molecular, and materials systems. It has the benefits of being noise resilient and only requires modest quantum resources on small quantum machines that can produce ac-

curate groundstate properties of systems not able to be simulated directly. We have implemented QEDFT for the prototypical Fermi-Hubbard lattice model and demonstrated that it is a powerful hybrid quantum/classical approach that can compete with state-of-the-art classical methods and outperform conventional variational quantum algorithms. QEDFT holds the potential to optimise the utility of near-term quantum machines for accurate simulations of many-body quantum systems such as materials and molecules.

Acknowledgements

We would like to thank the rest of the Phasecraft team for many helpful and insightful discussions. This work was supported by the Innovate UK (grant no. 44167).

Appendix

A Computational methods

For the VQE simulations, we implemented the Hamiltonian variational ansatz [43] which has been shown to be promising for solving the Fermi-Hubbard model [41]. The starting state was taken to be the groundstate of the $U = 0$ Fermi-Hubbard model which can be prepared efficiently on a quantum computer using Givens rotations [47] and the commuting sets were auto-generated using a greedy graph colouring algorithm. The quantum circuit simulations for VQE were run using the Julia package Yao [48]. Since all the simulations generated the exact VQE state, i.e. no measurements or noise, we were able to use Yao’s automatic differentiation framework to speed up calculations of the gradient to be used with the L-BFGS [49] optimiser in NLOpt [50].

To analyse the performance of QEDFT on quantum hardware, we were able to make use of previous Fermi-Hubbard VQE experiments that had been carried out on Google’s 23-qubit Rainbow chip [21]. The three instances of the model that were considered in the paper and that we consider here are: the 1×4 Fermi-Hubbard model with VQE depth 2; the 1×8 Fermi-Hubbard model with depth 1; and the 2×4 Fermi-Hubbard model with depth 1. For each of these models we generated a QEDFT XC potential, referred to as the QEDFT hardware functional, which is then used inside a DFT loop for the original homogeneous system and complementary inhomogeneous systems. Note that the ansatz that was run on the hardware is not identical to the ansatz for the exact simulations, which is why the hardware may sometimes produce different results to simulated VQE, up to noise.

The lattice DFT algorithm is implemented according to [Table 1](#) and the self consistent protocol is run, unless otherwise specified, for 500 DFT

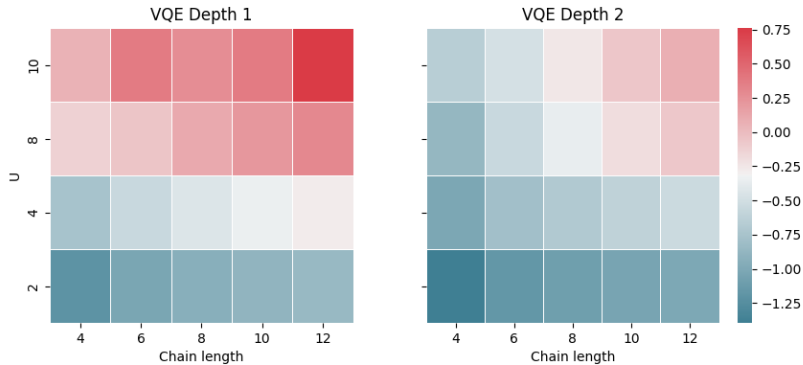


Figure 10: The \log_{10} Frobenius norm error between the VQE XC potential functionals and the exact functional for 1D Fermi-Hubbard models at different values of interaction strength U/t (where we take $t = 1$) and system size.

iterations using a density mixing of $\alpha = 0.95$ with the initial density ansatz being chosen such that it is proportional to the external potential.

B Error analysis of the XC functional

In Fig. 10 we provide a quantitative illustration of the error in the XC functional across varying interaction strengths and system sizes. To isolate errors from the splining procedure, we present the Frobenius norm error (on a \log_{10} scale) between the VQE XC potential functionals and the exact functional with respect to the discrete values that are computed. We confirm that VQE functionals decrease in accuracy for bigger systems sizes with larger U/t parameters and that increasing the number of VQE layers can significantly improve the quality of the underlying functional, especially in the high U/t (≈ 10) and large system size ($\approx 1 \times 12$) parameter regime of the 1D Hubbard model.

When U/t is smaller, i.e. ≤ 4 , it is sufficient to use a VQE functional of depth 1 for all system sizes up to 1×12 , as the overall error metric is on a similar scale as that for the VQE functionals of depth 2. Indeed, our results suggest that the XC functional in 1D is more sensitive to increases in the interaction strength than similar increases in the system size, indicating that there exists legitimate regions of applicability for low-depth VQE functionals in DFT computations. This bias is due to the structure of the ansatz circuit for VQE, that uses the non-interacting groundstate at $U = 0$ as a starting state. Potential improvements could be made by varying this ansatz.

In Fig. 11 we examine the effect that VQE depth has across a range of 2D system sizes. Similar to 1D, it is clear that the leading indicator

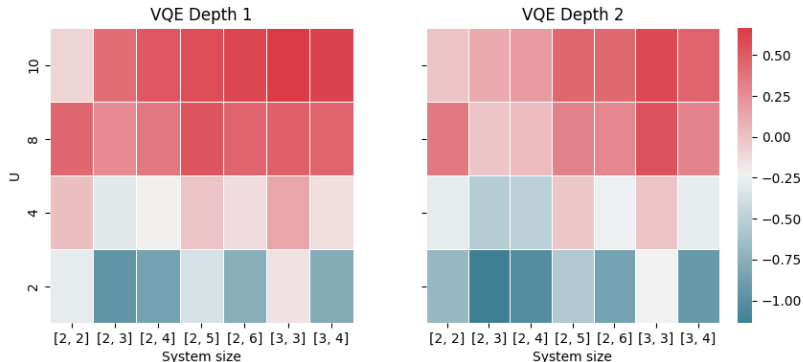


Figure 11: The \log_{10} Frobenius norm error between the VQE XC potential functionals and the exact functional for 2D Fermi-Hubbard models at different values of interaction strength U/t and system size $[n_x, n_y]$.

for quality in the VQE functional is the variational depth at which the quantum simulation is performed. While we observe that the 2D results do not see the same quality of improvements at VQE depth 2 as the 1D systems show, most notably in the $U \geq 8$ regions, we nevertheless do see consistent improvements over depth 1. This suggests that 2D VQE functionals may benefit, especially at larger interaction strengths, from using slightly larger circuit depths, or varying the circuit ansatz as discussed above. Similar to the 1D case, we see that for U values in the region of $U \leq 4$ it is sufficient to use VQE functionals of depth 1 in favour of depth 2 as they retain a similar accuracy.

C QEDFT in 1D

C.1 Emulation

In Fig. 12 we present QEDFT, DFT, VQE, and exact results for the 1×12 Fermi-Hubbard model with an external quadratic potential $v_i^{ext} = (i-1)^2/L$ with $L = 12$. The model parameters are $U = 4$, $t = 1$, and $N_e = 6$ (i.e. quarter-filling). The exact results are found using exact diagonalisation of the full system.

Fig. 12 shows the convergence of the energy and the corresponding final density for all methods, with the final errors displayed in Table 3. Considering the energetics, the QEDFT method clearly achieves better accuracy than both DFT HF alone (Hartree Fock - which by definition has no discontinuity) and pure quantum VQE alone and converges after ~ 100 iterations to δ , the DFT self-consistency criteria, within machine precision. Fig. 12 also highlights that despite only having access to qualitatively accurate XC energy functionals via VQE simulations it is possible to outperform popular

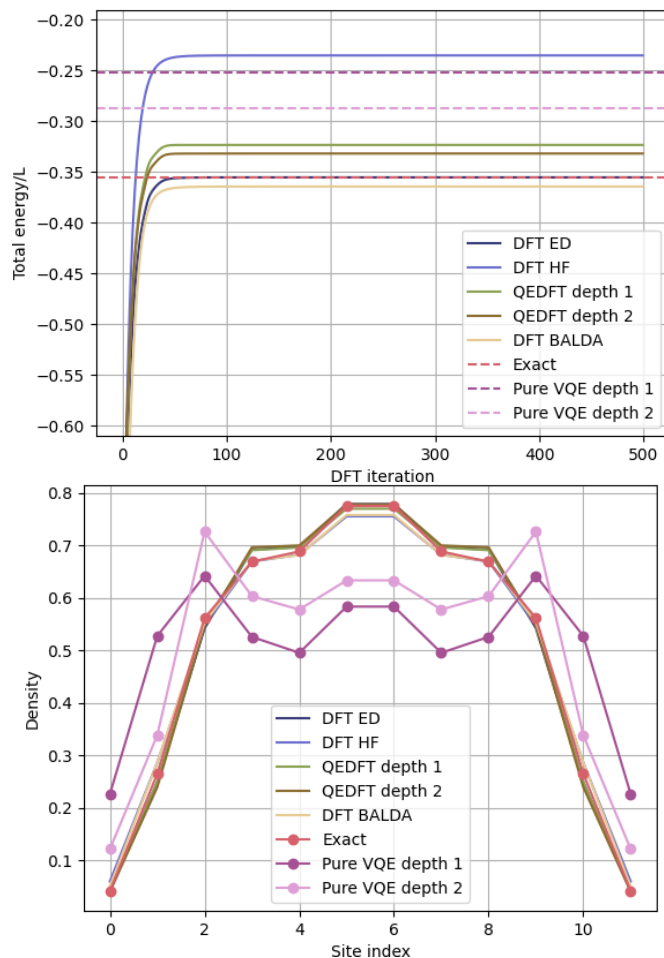


Figure 12: The 1×12 Fermi Hubbard model for $U = 4$ and at quarter-filling with an external quadratic potential. The top plot illustrates the convergence of the total energy per lattice site within the DFT loop. The bottom plot displays the density as predicted using different DFT functionals and the corresponding exact methods.

classical approximations and/or purely quantum approaches.

Similarly the density also converges to machine precision in the DFT self-consistency criteria. The pure VQE methods struggle to reproduce the sharp central peak at the centre of the chain generated by the external quadratic potential and is also considerably erroneous near the boundaries. The QEDFT approach captures these features well over the entire chain and are qualitatively indistinguishable from the state-of-the-art classical methods. Moreover in [Table 3](#) the errors of the groundstate density from QEDFT are comparable to all of the classical methods. Notably the QEDFT density at depth 1 is more accurate than at depth 2 and we attribute this difference

Method	Δn	ΔE
Pure VQE depth 1	0.635	0.10
Pure VQE depth 2	0.388	0.067
QEDFT depth 1	0.043	0.031
QEDFT depth 2	0.06	0.023
DFT HF	0.052	0.11
DFT BALDA	0.044	0.009
DFT ED	0.050	0.0005

Table 3: The Frobenius error norm in density $\Delta n = \sqrt{\sum_i^L |n_{i,\text{approx}} - n_{i,\text{EXACT}}|^2}$ and error in energy $\Delta E = |E_{\text{approx}} - E_{\text{EXACT}}|$ after 500 DFT iterations with respect to the exact groundstate.

to the interpolation scheme used for the XC energy and potential, which we expect to disappear at higher depths. From this result we see that QEDFT not only can predict the groundstate energy accurately, it is also well suited to predicting the groundstate density, and in particular it is far superior than using pure VQE alone.

We extend our analysis to understand how QEDFT deals with the impact of changing the type of external potential for the 1×12 Fermi-Hubbard model. In Fig. 13 we highlight the DFT groundstate properties and how they converge for (i) no external potential, (ii) a confining quadratic potential and (iii) a single impurity potential placed near the centre of the chain. In the top panel of Fig. 13 we show the groundstate density prediction across all potentials for all methods. The observations we made for the quadratic potential also apply to the case of no potential as well as an impurity in the centre of the system, i.e the densities from QEDFT are qualitatively always more accurate than pure quantum VQE and comparable to the classical state-of-the-art.

Focusing on the case of no potential, which is equivalent to the homogeneous problem from which the XC functionals are generated, we emphasise that even here the QEDFT approach yields better groundstate density estimates than VQE alone. That is to say, by first doing a VQE computation and then doing a QEDFT computation using the VQE data we are able to arrive at a more accurate description of the groundstate density. This suggest a wide range of applicability of the QEDFT approach for general homogeneous and inhomogeneous 1D Fermi-Hubbard Hamiltonians, where the QEDFT functionals can provide an avenue for using small quantum machines to improve over pure VQE as well as classical approximations.

The strength of interactions U/t determines how correlated the groundstate of the Fermi-Hubbard model is, which is largely captured within the XC potential V_{XC} . As U/t is increased, classical HF theory breaks down in its ability to describe groundstate properties as it explicitly sets the XC po-

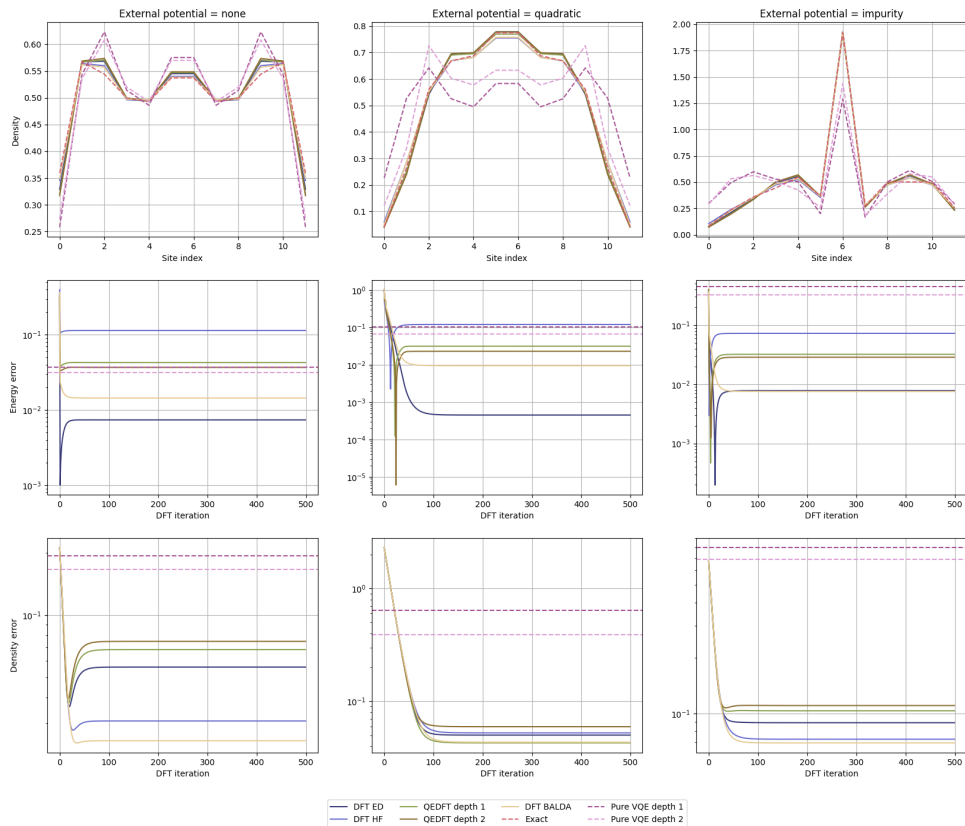


Figure 13: The 1×12 Fermi Hubbard model for $U = 4$ and at quarter-filling for different external potentials (column-wise). The first row compares the DFT densities compared to the exact predictions. The second row monitors the convergence of the difference in total energy against the exact solution over the duration of the DFT computation. The third row monitors the convergence of the difference in total density against the exact solution over the duration of the DFT computation.

tential to zero and reduces the Fermi-Hubbard problem into a purely single particle problem in the absence of exchange and correlation. In Fig. 14 we examine the effect of increasing U/t on the groundstate energy and density for the 1×12 system at quarter-filling within the same confining quadratic potential. This is a direct probe of how well the QEDFT functional can encapsulate XC effects.

In Fig. 12 and Fig. 13, we noticed that while QEDFT always outperforms VQE in accuracy for both energy and density metrics, it competed with all classical methods, importantly including HF for the density. In Fig. 14 we see that when $U/t \geq 4$, QEDFT consistently is more accurate than HF for both the energy and the density. Indeed, as U/t increases, the HF approximation becomes less well justified due to the presence of correlations. On

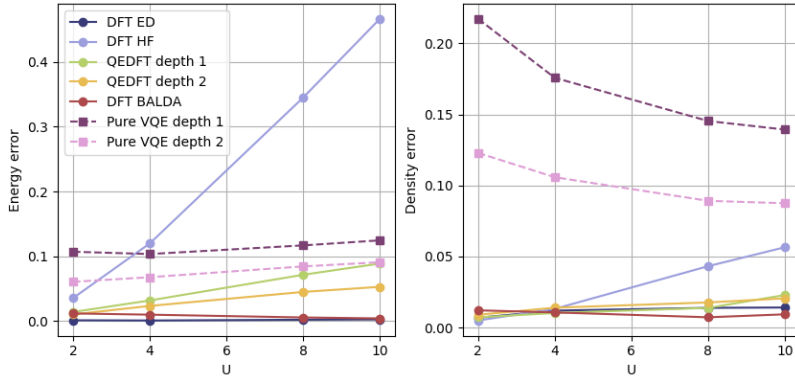


Figure 14: The 1×12 Fermi Hubbard model at quarter-filling with a quadratic external potential and its respective errors in energy (left panel) and density (right panel) for different interaction strengths. All simulations use DFT apart from the dashed lines.

the other hand, when U/t is small the presence of interactions is weaker and the validity of HF is evidenced by its capacity to predict the groundstate density, despite the energy being vastly overestimated. Importantly, this acts as a demonstration that QEDFT functionals, even those which are generated from low-depth VQE circuits, are able to reproduce essential features of correlation that are needed to describe the Mott insulating phase of the Fermi-Hubbard model.

C.1.1 Finite size scaling

Another pertinent question related to the scalability of the QEDFT method is if the performance of the functional improves as a function of system size. We probe this question by using functionals generated on 1×6 and 1×12 homogeneous systems applied to 1×12 inhomogeneous models with a quadratic potential. In the top panel of Fig. 15 we see that the error in the energy when using different functionals manifestly improves for the ED functional, indicating that the quality of the solution gets better by using DFT functionals which are generated on larger grids. We note that the DFT HF and DFT BALDA solutions in both of these cases are the same, as they are not sensitive to system size. Notably, the QEDFT energetics do not demonstrably improve, rather slightly worsen, when increasing the size of the system used to obtain the functional. We attribute this behaviour to the worsening of the VQE algorithm with system size at fixed depth, and expect this to be resolved by increasing the ansatz depth.

However, in the bottom panel of Fig. 15 we find that the total error of the density undeniably improves as the system on which the functional

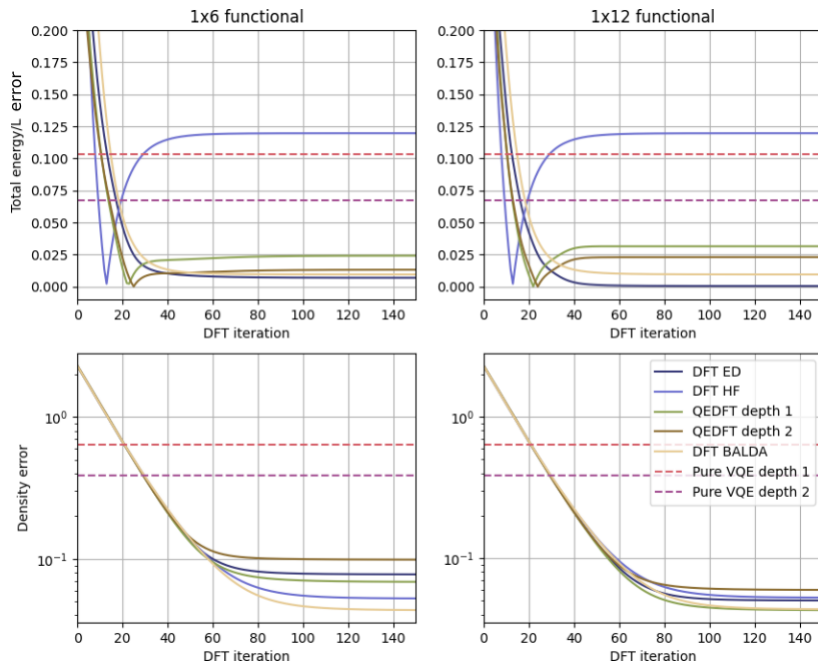


Figure 15: Performance of the finite size scaling of XC functionals in the convergence of the total energy error (top panel) and density error (bottom panel) with respect to the exact solution for the quadratic external potential. Left column are the results produced with 1×6 XC potential. Right column are the results produced with 1×12 XC potential.

is used increases. There is a systematic reduction of the error for each approximation, with BALDA being the most accurate method to predict the density. We note that the quality of these results will be dependent on the inhomogeneous models studied and their parameter settings, but largely we have identified that the above trends hold across the various systems we have examined.

C.2 Hardware

We analyse the effect of this noise by implementing first the QEDFT functional for the 1×8 model for different homogeneous and inhomogeneous 1×8 Fermi-Hubbard models. We choose this model as it represents the case where the XC potential possesses significant hardware noise, in order to assess how this manifests in the DFT results. The results are shown in Fig. 16. Despite the presence of noise, the hardware data achieves more accurate results than brute force simulated VQE at depth 1 and 2 in all scenarios, for both the energy and density. The QEDFT hardware energetics consistently achieve accuracies relative to the true energy between 10^{-1} and 10^{-2} , which is significantly better than the classical HF results. While

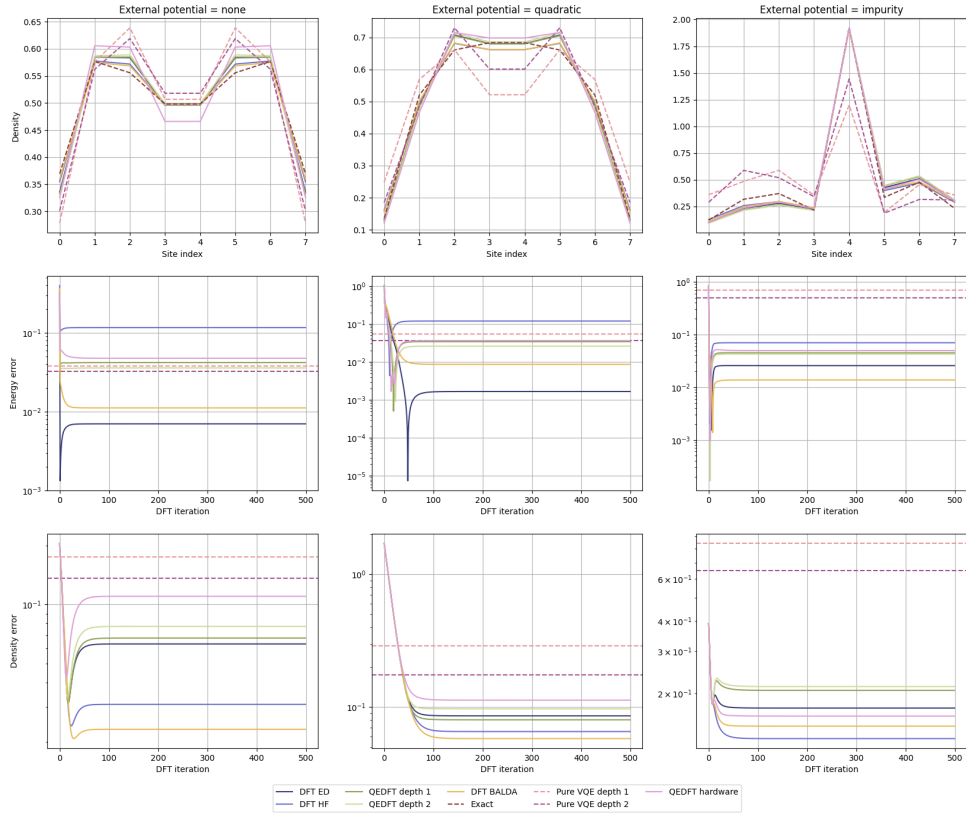


Figure 16: The 1×8 Fermi Hubbard model for $U = 4$ and at quarter-filling for different external potentials (column-wise) including results on hardware. The first row compares the DFT densities compared to the exact predictions. The second row monitors the convergence of the difference in total energy against the exact solution over the duration of the DFT computation. The third row monitors the convergence of the difference in total density against the exact solution over the duration of the DFT computation.

the QEDFT hardware densities do not outperform the classical HF densities, they are certainly similar in accuracy to the QEDFT simulated functionals, which can be improved by including more variational layers. Indeed, even though there is the clear presence of noise in the QEDFT hardware functional, manifest in both the raw data as well its interpolation, we show that its subsequent application in a DFT simulation is largely oblivious to these details for the model parameters we have considered.

D QEDFT in 2D

D.1 Emulation

We now proceed with the DFT analysis of Fermi-Hubbard models in 2D, beginning with the energy convergence of the DFT energy, presented in Fig. 17 for the 3×3 system with $U/t = 10$ at quarter filling. We consider the homogeneous model as well as the inhomogeneous system with an impurity potential embedded in a random background at the $(1, 2)$ site.

For the homogeneous model we observe that the convergence of DFT energy is initially unstable, as evidenced by the jagged spikes for the first 50 iterations. This behaviour is present in all functionals studied, indicating that this instability is not associated with the particular form of the XC potential but rather the stability of the single particle Kohn-Sham approach for the chosen parameter regime. A high density mixing parameter ($\alpha = 0.95$) ensures that early instabilities cannot propagate towards erroneous fixed points. However, inhomogeneities introduce more noticeable instabilities in the DFT algorithm, as evidenced by the jaggedness of the energy convergence around a fixed value. While not severe in this case, a combination of more accurate XC interpolation methods and higher density mixing parameters should remove convergence to multiple fixed points.

It is clear that in all cases using a VQE approach is superior to Hartree Fock, which for example has an error in the converged energy of $\approx 44\%$ for the homogeneous model, in contrast to the most accurate VQE method (QEDFT at depth 2) $\approx 6\%$. Indeed, we further see that QEDFT at depth 2 attains an accuracy closer to the exact solution than pure VQE alone, which is not achieved at QEDFT depth 1. In contrast to the 1D results, this suggests that going beyond depth 1 QEDFT functionals is not only beneficial, but also necessary, to improve upon using pure VQE. Finally, the ED functional produces the groundstate energy with an error of $\approx 0.1\%$, indicating that the local density approximation when sampled at the converged density produces a good, but not exact, estimate of the groundstate energy for 2D systems also.

In Fig. 18 we analyse converged groundstate densities for the inhomogeneous 3×3 system by presenting the site density percentage error with the groundstate density,

$$\Delta n_{ij} = \frac{|n_{ij}^{\text{approx}} - n_{ij}^{\text{exact}}|}{n_{ij}^{\text{exact}}}. \quad (40)$$

We arrive at a set of slightly different conclusions for the DFT groundstate densities as compared to the energies. For the densities, the DFT methods are always more reliable than pure VQE, which produces errors per site that are mostly all above 0.1% . QEDFT at depth 2 highly resembles the DFT ED and DFT HF solutions, indicating that low-depth

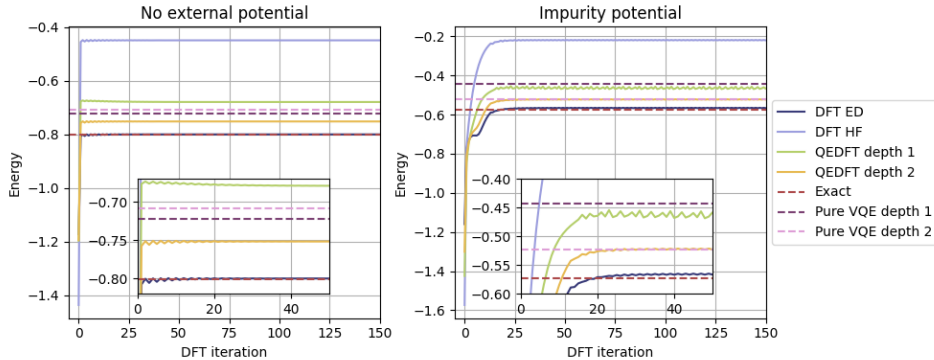


Figure 17: The DFT energy convergence 3×3 Fermi Hubbard model for $U/t = 10$ and at quarter-filling for no external potential and an impurity potential at the $(1, 2)$ site. Dashed lines represent non DFT calculations, which are either the exact solution or pure VQE emulations.

QEDFT methods can compete with classical state-of-the-art approaches for predicting the groundstate density in 2D. Moreover, despite potential errors arising in the interpolation of the XC potential due to rogue data points, i.e. as seen in Fig. 9 for the 3×3 case, we see that the DFT algorithm can be robust against these, depending on where the density is sampled. If the curvature of the underlying function is non-trivial, which it is for the 3×3 system, improvements can be made by using denser meshes to assist the interpolated XC potential and prevent DFT from driving the density to a result that is further away from the exact one, but are not necessary for this inhomogeneous model.

To quantify this error further we study the effect of varying U/t on the absolute errors with respect to the groundstate energies and densities for the quarter-filled 3×3 inhomogeneous impurity system, illustrated in Fig. 19. The results for the energetics are reminiscent of those presented for 1D systems in Fig. 14. The density results, however, deviate significantly from what we observed in 1D. Indeed, as U/t increases the density error decreases, which is opposite to the trend we observed for the 1D quadratic potential. Even at low U , the DFT ED functional does not reproduce the exact solution, indicating that the LDA approximation for the 2D Fermi Hubbard model at low U/t is not as reliable as in 1D for predicting the groundstate density. Generally speaking, the DFT methods, and in particular the QEDFT functionals, always provide more reliable densities than pure VQE alone across all values of U/t , except at $U/t = 2$, where pure VQE at depth 2 is the most accurate approach.

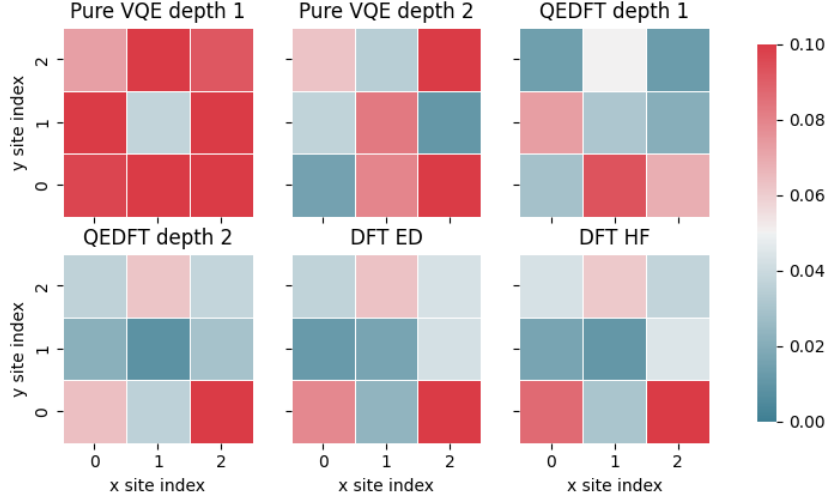


Figure 18: The per site density percentage error Eq. (40) for the 3×3 Fermi Hubbard model with impurity at site $(1, 2)$ for $U/t = 8$. Pure VQE methods are highlighted in the top panel, while the other methods use DFT.

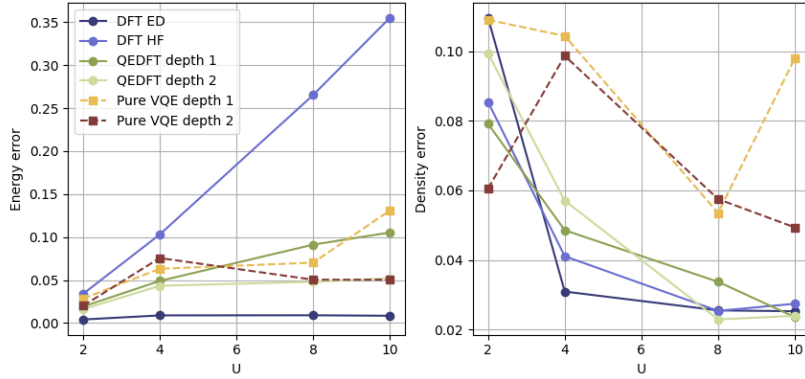


Figure 19: The 3×3 Fermi Hubbard model at quarter-filling with an impurity potential at the $(1, 2)$ site and its respective errors in energy (left panel) and density (right panel) for different interaction strengths. All simulations use DFT apart from the dashed lines.

D.1.1 Finite size scaling

We now revisit examining in 2D how well QEDFT scales as the functionals used are increased in the system size. In Fig. 20 we show that studying the inhomogeneous 2×4 Fermi-Hubbard system with an impurity at site $(1, 2)$ improves considerably when going from a functional generated on a 2×2

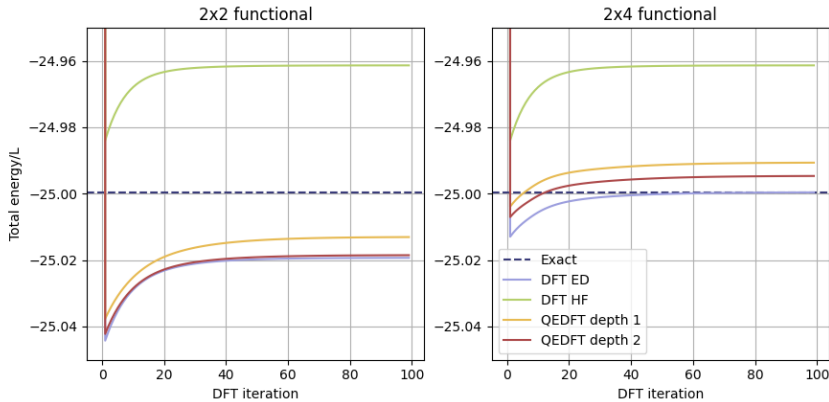


Figure 20: Comparing the performance of the 2×2 and 2×4 XC functional, for a 2×4 model with an impurity at site $(1, 2)$. The energy per site is plotted against the DFT iteration.

lattice, as compared to using a functional from a 2×4 system. Notably, the DFT ED results converge to the exact method using the 2×4 functional, demonstrating the utility of how the functional can scale with system size. Moreover, the QEDFT energetics also converge to values which are closer to the exact value, but are not as close as DFT ED. The pure VQE energetics are not shown, as they incur an error of approximately $\sim 20\%$, as opposed to the DFT methods, which are all within the region of less than $\sim 0.2\%$. In contrast to the 1D results in Fig. 15, for 2D we did not observe a significant improvement related to the density in 2D.

D.2 Hardware

We study the 2×4 Fermi-Hubbard system using the hardware functional without an external potential and in the presence of a single impurity at the $(1, 1)$ site embedded in a disordered external potential. The results are shown in Fig. 21 and Fig. 22. For both the homogeneous and inhomogeneous models we see that that all DFT methods are stable, in contrast to the 3×3 simulations. The origin of these differences is possibly related to the behaviour of the XC functional near half-filling as we presented in Fig. 9, which is noticeably worse for the square 3×3 lattice than for rectangular lattices. Indeed, this indicates that errors originating from the splining of the XC functional may have less of an impact on the stability of the DFT algorithm than absolute error of the raw data to the exact reference values.

We also find that the DFT hardware energetics, while consistently better than classical HF, is either slightly worse or essentially no better than exact emulations of pure VQE. As there is no hardware data for the direct implementation of VQE for these target problems we cannot directly com-

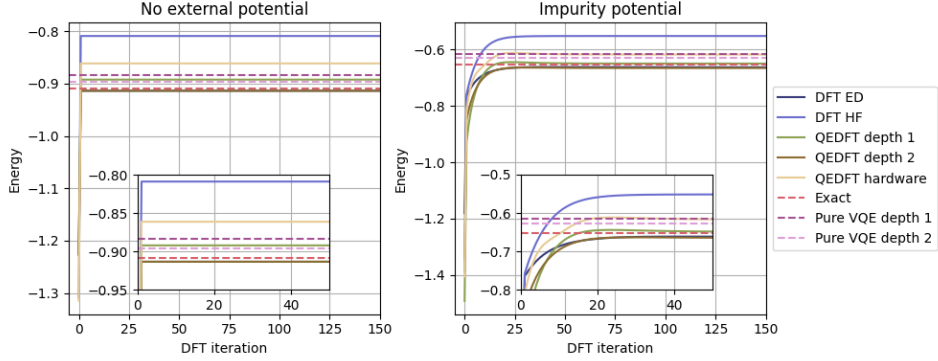


Figure 21: The DFT energy convergence 2×4 Fermi Hubbard model for $U/t = 4$ and at quarter-filling for no external potential and an impurity potential at the $(1, 1)$ site using the hardware data. Dashed lines represent non DFT calculations, which are either the exact solution or pure VQE emulations.

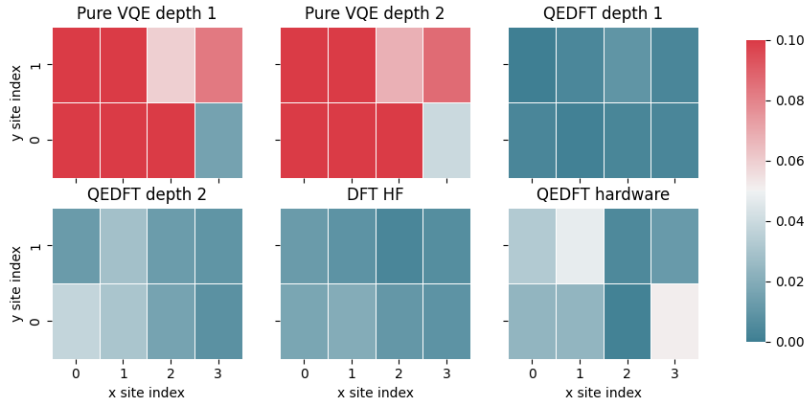


Figure 22: The per site density percentage error Eq. (40) for the quarter-filled 2×4 Fermi Hubbard model with impurity at site $(1, 2)$ for $U/t = 4$ including hardware data.

pare DFT VQE to pure VQE on hardware, but anticipate DFT VQE to outperform the latter as we consistently observed that in emulation.

The hardware data is also used to assess the accuracy of DFT for the groundstate density of the inhomogeneous 2×4 problem in Fig. 22. Interestingly, the hardware functional produces groundstate densities a lot closer than pure VQE emulation, having a per-site percentage error of less than 0.1% for all sites, while most sites predicted with the VQE emulation have errors greater than 0.1%. As was observed for the emulations of the 3×3 model, the DFT methods based on VQE are comparable to classical

HF, which is also true for the hardware functional in this case. Notably, the QEDFT depth 1 densities produce results that are closer to the true solution than QEDFT depth 2. Indeed, this is also reflected in the accuracy of the energetics, and is related to the quality of the interpolation method performed. Due to the finite data set over which the XC functional is constructed, it is possible to introduce error at higher depths within the interpolated region if the spacing is not large enough, with respect to lower-depth results. Therefore, we anticipate that classical improvements to the interpolation protocol of QEDFT should make it possible to obtain groundstate properties closer to the true results.

References

- [1] L. Clinton et al. ‘Towards near-term quantum simulation of materials’. *Nature Communications* 15.1 (2024), p. 211.
- [2] P. Hohenberg and W. Kohn. ‘Inhomogeneous Electron Gas’. *Phys. Rev.* 136 (3B 1964), B864–B871.
- [3] W. Kohn and L. J. Sham. ‘Self-Consistent Equations Including Exchange and Correlation Effects’. *Phys. Rev.* 140 (4A 1965), A1133–A1138.
- [4] N. Schuch and F. Verstraete. ‘Computational complexity of interacting electrons and fundamental limitations of density functional theory’. en. *Nature Physics* 5.10 (2009), pp. 732–735.
- [5] R. Peverati and D. G. Truhlar. ‘Quest for a universal density functional: the accuracy of density functionals across a broad spectrum of databases in chemistry and physics’. *Philosophical Transactions of the Royal Society A: Mathematical, Physical and Engineering Sciences* 372.2011 (2014), p. 20120476.
- [6] N. Mardirossian and M. Head-Gordon. ‘Thirty years of density functional theory in computational chemistry: an overview and extensive assessment of 200 density functionals’. *Molecular Physics* 115.19 (2017), pp. 2315–2372.
- [7] D. M. Ceperley and B. J. Alder. ‘Ground State of the Electron Gas by a Stochastic Method’. *Phys. Rev. Lett.* 45 (7 1980), pp. 566–569.
- [8] M. A. Marques, M. J. Oliveira and T. Burnus. ‘Libxc: A library of exchange and correlation functionals for density functional theory’. *Computer Physics Communications* 183.10 (2012), pp. 2272–2281.
- [9] N. A. Lima, M. F. Silva, L. N. Oliveira and K. Capelle. ‘Density Functionals Not Based on the Electron Gas: Local-Density Approximation for a Luttinger Liquid’. *Phys. Rev. Lett.* 90 (14 2003), p. 146402.

- [10] R. Haunschild, A. Barth and B. French. ‘[A comprehensive analysis of the history of DFT based on the bibliometric method RPYS](#)’. *Journal of Cheminformatics* 11.1 (2019), p. 72.
- [11] R. O. Jones. ‘[Density functional theory: Its origins, rise to prominence, and future](#)’. *Rev. Mod. Phys.* 87 (3 2015), pp. 897–923.
- [12] N. Marzari, A. Ferretti and C. Wolverton. ‘[Electronic-structure methods for materials design](#)’. *Nature Materials* 20.6 (2021), pp. 736–749.
- [13] F. Tran, J. Stelzl and P. Blaha. ‘[Rungs 1 to 4 of DFT Jacob’s ladder: Extensive test on the lattice constant, bulk modulus, and cohesive energy of solids](#)’. *The Journal of Chemical Physics* 144.20 (2016), p. 204120.
- [14] A. Georges, G. Kotliar, W. Krauth and M. J. Rozenberg. ‘[Dynamical mean-field theory of strongly correlated fermion systems and the limit of infinite dimensions](#)’. *Rev. Mod. Phys.* 68 (1 1996), pp. 13–125.
- [15] T. Kotani, M. van Schilfgaarde and S. V. Faleev. ‘[Quasiparticle self-consistent *GW* method: A basis for the independent-particle approximation](#)’. *Phys. Rev. B* 76 (16 2007), p. 165106.
- [16] A. Peruzzo, J. McClean, P. Shadbolt, M.-H. Yung, X.-Q. Zhou, P. J. Love, A. Aspuru-Guzik and J. L. O’Brien. ‘[A variational eigenvalue solver on a photonic quantum processor](#)’. *Nature Communications* 5.1 (2014), p. 4213.
- [17] J. R. McClean, J. Romero, R. Babbush and A. Aspuru-Guzik. ‘[The theory of variational hybrid quantum-classical algorithms](#)’. *New Journal of Physics* 18.2 (2016), p. 023023.
- [18] M. Cerezo et al. ‘[Variational quantum algorithms](#)’. *Nature Reviews Physics* 3.9 (2021), pp. 625–644.
- [19] K. Bharti et al. ‘[Noisy intermediate-scale quantum algorithms](#)’. *Rev. Mod. Phys.* 94 (1 2022), p. 015004.
- [20] J. Tilly et al. ‘[The Variational Quantum Eigensolver: A review of methods and best practices](#)’. *Physics Reports* 986 (2022), pp. 1–128.
- [21] S. Stanisic, J. L. Bosse, F. M. Gambetta, R. A. Santos, W. Mroczkiewicz, T. E. O’Brien, E. Ostby and A. Montanaro. ‘[Observing ground-state properties of the Fermi-Hubbard model using a scalable algorithm on a quantum computer](#)’. *Nature Communications* 13.1 (2022), p. 5743.
- [22] M. Rossmannek, P. K. Barkoutsos, P. J. Ollitrault and I. Tavernelli. ‘[Quantum HF/DFT-embedding algorithms for electronic structure calculations: Scaling up to complex molecular systems](#)’. *The Journal of Chemical Physics* 154.11 (2021), p. 114105.

- [23] H. Ma, M. Govoni and G. Galli. ‘Quantum simulations of materials on near-term quantum computers’. en. *npj Computational Materials* 6.1 (2020), p. 85.
- [24] B. Huang, M. Govoni and G. Galli. ‘Simulating the Electronic Structure of Spin Defects on Quantum Computers’. *PRX Quantum* 3 (1 2022), p. 010339.
- [25] B. Huang, N. Sheng, M. Govoni and G. Galli. ‘Quantum Simulations of Fermionic Hamiltonians with Efficient Encoding and Ansatz Schemes’. *Journal of Chemical Theory and Computation* 19.5 (2023), pp. 1487–1498.
- [26] J. R. McClean, M. E. Kimchi-Schwartz, J. Carter and W. A. de Jong. ‘Hybrid quantum-classical hierarchy for mitigation of decoherence and determination of excited states’. *Phys. Rev. A* 95 (4 2017), p. 042308.
- [27] R. Hatcher, J. A. Kittl and C. Bowen. ‘A Method to Calculate Correlation for Density Functional Theory on a Quantum Processor’. *arXiv:1903.05550 [quant-ph]* (2019).
- [28] T. E. Baker and D. Poulin. ‘Density functionals and Kohn-Sham potentials with minimal wavefunction preparations on a quantum computer’. en. *Physical Review Research* 2.4 (2020), p. 043238.
- [29] C. D. Pemmaraju and A. Deshmukh. ‘Levy-Lieb embedding of density-functional theory and its quantum kernel: Illustration for the Hubbard dimer using near-term quantum algorithms’. *Phys. Rev. A* 106 (4 2022), p. 042807.
- [30] B. Senjean, S. Yalouz and M. Saubanère. ‘Toward density functional theory on quantum computers?’ *SciPost Phys.* 14 (2023), p. 055.
- [31] O. Gunnarsson and K. Schönhammer. ‘Density-Functional Treatment of an Exactly Solvable Semiconductor Model’. *Phys. Rev. Lett.* 56 (18 1986), pp. 1968–1971.
- [32] G. Xianlong, M. Polini, M. P. Tosi, V. L. Campo, K. Capelle and M. Rigol. ‘Bethe ansatz density-functional theory of ultracold repulsive fermions in one-dimensional optical lattices’. *Phys. Rev. B* 73 (16 2006), p. 165120.
- [33] K. Capelle and V. L. Campo. ‘Density functionals and model Hamiltonians: Pillars of many-particle physics’. *Physics Reports* 528.3 (2013), pp. 91–159.
- [34] D. J. Carrascal, J Ferrer, J. C. Smith and K Burke. ‘The Hubbard dimer: a density functional case study of a many-body problem’. *Journal of Physics: Condensed Matter* 27.39 (2015), p. 393001.

- [35] V. V. França, J. P. Coe and I. D’Amico. ‘Testing density-functional approximations on a lattice and the applicability of the related Hohenberg-Kohn-like theorem’. *Scientific Reports* 8.1 (2018), p. 664.
- [36] M. Ijäs and A. Harju. ‘Lattice density-functional theory on graphene’. *Phys. Rev. B* 82 (23 2010), p. 235111.
- [37] M. Bogojeski, L. Vogt-Maranto, M. E. Tuckerman, K.-R. Müller and K. Burke. ‘Quantum chemical accuracy from density functional approximations via machine learning’. *Nature Communications* 11.1 (2020), p. 5223.
- [38] L. O. Wagner, T. E. Baker, E. M. Stoudenmire, K. Burke and S. R. White. ‘Kohn-Sham calculations with the exact functional’. *Phys. Rev. B* 90 (4 2014), p. 045109.
- [39] J. Kirkpatrick et al. ‘Pushing the frontiers of density functionals by solving the fractional electron problem’. *Science* 374.6573 (2021), pp. 1385–1389.
- [40] J. Nelson, R. Tiwari and S. Sanvito. ‘Machine learning density functional theory for the Hubbard model’. *Phys. Rev. B* 99 (7 2019), p. 075132.
- [41] C. Cade, L. Mineh, A. Montanaro and S. Stanisic. ‘Strategies for solving the Fermi-Hubbard model on near-term quantum computers’. *Phys. Rev. B* 102 (23 2020), p. 235122.
- [42] A. Montanaro and S. Stanisic. ‘Compressed variational quantum eigensolver for the Fermi-Hubbard model’. *arXiv:2006.01179 [quant-ph]* (2020).
- [43] D. Wecker, M. B. Hastings and M. Troyer. ‘Progress towards practical quantum variational algorithms’. *Phys. Rev. A* 92 (4 2015), p. 042303.
- [44] M. J. P. Hodgson, E. Kraisler, A. Schild and E. K. U. Gross. ‘How Interatomic Steps in the Exact Kohn–Sham Potential Relate to Derivative Discontinuities of the Energy’. *The Journal of Physical Chemistry Letters* 8.24 (2017), pp. 5974–5980.
- [45] A. V. Ivanov, C. Sünderhauf, N. Holzmann, T. Ellaby, R. N. Kerber, G. Jones and J. Camps. ‘Quantum computation for periodic solids in second quantization’. *Phys. Rev. Res.* 5 (1 2023), p. 013200.
- [46] J. P. Perdew, K. Burke and M. Ernzerhof. ‘Generalized Gradient Approximation Made Simple’. *Phys. Rev. Lett.* 77 (18 1996), pp. 3865–3868.
- [47] Z. Jiang, K. J. Sung, K. Kechedzhi, V. N. Smelyanskiy and S. Boixo. ‘Quantum Algorithms to Simulate Many-Body Physics of Correlated Fermions’. *Phys. Rev. Appl.* 9 (4 2018), p. 044036.

- [48] X.-Z. Luo, J.-G. Liu, P. Zhang and L. Wang. ‘Yao.jl: Extensible, Efficient Framework for Quantum Algorithm Design’. *Quantum* 4 (2020), p. 341.
- [49] D. C. Liu and J. Nocedal. ‘On the limited memory BFGS method for large scale optimization’. *Mathematical Programming* 45 (1989), pp. 503–528.
- [50] S. G. Johnson. ‘The NLOpt nonlinear-optimization package’. <https://github.com/stevengj/nlopt>. 2007.